The Pennsylvania State University

The Graduate School

DEVELOPMENT OF A BROADBAND RECEIVER FOR A QUADRUPOLE RESONANCE (QR) DETECTION SYSTEM

A Thesis in

Electrical Engineering

by

Bianca Borda

Submitted in Partial Fulfillment
of the Requirements
for the Degree of

Master of Science

December 2022

The thesis of Bianca Borda was reviewed and approved by the following:

Jeffrey L. Schiano
Associate Professor of Electrical Engineering
Thesis Advisor

Julio Urbina
Associate Professor of Electrical Engineering
Committee Member

Thomas La Porta
Evan Pugh Professor
Director of Electrical Engineering and Computer Science

Abstract

This thesis designs a broadband receiver for quadrupole resonance (QR) detection systems. A QR detection system can reveal the presence of concealed materials such as explosives and narcotics. A QR system generates a series of radio-frequency (RF) pulses at a transition frequency of a target material, and if present, the target admits an RF signal at the transition frequency between the applied RF pulses. QR transition frequencies are unique to the target compound and range from about 400 kHz to 5 MHz.

As the QR response is weak, conventional QR detection systems noise match an inductive sensor to a low-noise preamplifier. This approach has two drawbacks. First, the noise-matching network must be re-tuned for each target frequency, thereby increasing the time to scan for multiple targets. Second, as the inductive sensor typically has a small real resistance, when in combination with the noise-matching network, a resonant circuit with a high-quality factor is formed. The applied RF pulses induce ringing in the tuned inductive sensor that introduces an undesirable dead time during reception of the QR response, as it is much smaller than the ringing amplitude. This thesis investigates an alternative broadband approach where the inductive sensor is connected to a broadband receiver that does not require tuning and which does not form a resonant circuit that can ring in response to RF pulses. While the predicted noise figure for the broadband receiver is larger than that of the noise-matched receiver, the reduction of dead time allows the spacing between RF pulses to be reduced. This in turn, increases the amplitude of the QR response, so that the measurement signal-to-noise ratio increases, despite the increase in receiver noise factor. Circuit simulations and a QR response simulation are used to predict the increase in measurement signal-to-noise ratio provided by the proposed broadband receiver design.

Table of Contents

List of Figures

List of Tables

Acknowledgments

I would like to thank my research advisor, Dr. Schiano for giving me the opportunity to work in his lab. In addition, he taught some of my first control system classes at Penn State that ultimately led me to pursue graduate school. Dr. Schiano's passion and energy for Electrical Engineering is truly one of a kind and I am fortunate to have worked with him for the last 3 years.

I would also like to thank Dr. Urbina. As my honor's advisor, he was the first faculty member I met at Penn State and has seen my academic growth from my first year. During my time at Penn State, Dr. Urbina's calm nature has reassured me through many obstacles and gave me the confidence I have today. Some people think a good advisor is just someone to that knows how to answer your questions about school or research, but I have learned how impactful it is to have an advisor that believes in you and encourages you to take opportunities as they come. I am lucky to have had an advisor as kind-hearted as Dr. Urbina for the last 5 years.

To my lab mates, I am thankful our time at Penn State made us cross paths. The late nights in the lab and supporting one another is an experience I will never forget. As my fellow women in engineering, you both are inspiring and I cannot wait to see what your future holds.

Lastly, to my family, every academic achievement of mine is due to your support. Between my time at school or time during breaks, your encouragement and guidance has allowed me to pursue academic opportunities I have dreamed about.

Chapter 1
Problem Statement

1.1 QR Detection Systems

QR detection systems provide a means to detect concealed materials such as explosives and narcotics [1]. Short-range remote explosives detection using nitrogen-14 QR transitions was first demonstrated nearly sixty years ago in an effort to discover improvised explosive devices used against American soldiers in the Vietnam Conflict [2, 3]. The North Vietnamese forces would recycle American munitions as satchel charges and liberally seed roadways with both satchel charges and decoys. Metal detectors were unable to identify the satchels loaded with explosives. Despite the demonstration of a QR system that could detect the explosive TNT three feet from a search coil, funding for the project was eliminated with the withdrawal of American forces from Vietnam in 1973. Fifteen years later, Pan Am Flight 103 was destroyed and the remains landed in Lockerbie, Scotland. The ensuing investigation revealed that 340 to 450 g of plastic explosive had been detonated in the airplane's forward cargo hold, triggering a sequence of events that destroyed the aircraft. Investigators at the Naval Research Laboratory noted that x-ray detection systems and magnetometers used at aviation security checkpoints could not reveal the presence of the plastic explosive. To overcome this deficiency, they developed QR systems in the early 1990s for detecting sub-kilogram quantities of explosives concealed within suitcases and passenger clothing [6–9]. Since that time, there have been many attempts to commercialize QR detection technology, but to date, none have produced a viable detection system [10, 11]. This section briefly describes the QR detection process, while Section 1.2 summarizes the challenges that continue to impede commercialization. Lastly, Section 1.3 summarizes the goals of the design presented in this thesis.

Quadrupole resonance (QR) spectroscopy is a promising technology for detecting

concealed contraband, such as explosives and narcotics, as it is non-invasive and uniquely identifies compounds based on their spectra [1]. The underlying science is a derivative of research in magnetic resonance (MR) spectroscopy [4]. For a material to have a QR response, it must have nuclei that have an electric quadrupole moment and a spin angular momentum quantum number equal, or greater than, one. The electrostatic interaction between the electric quadrupole moment of nuclei and the electric field gradient produced by surrounding electronic charges, causes the nuclei to rotate so that their electric quadrupole moment aligns along the direction of the largest electric field gradient. Because the nuclei must also possess spin angular momentum, the electrostatic energy levels are quantized. The position of the nuclei can be perturbed by applying a rotating magnetic field at a transition frequency corresponding to the difference between the energy levels of the electrostatic interaction. In practice, a rotating field is generated by applying a radio frequency pulse at the transition frequency to a probe coil. Since the nuclei also possess intrinsic angular momentum, it precesses about the axis of the largest electric field gradient. The magnetic moment of the processing nuclei induces a voltage in the probe coil at the transition frequency, thereby revealing the presence of the material. As the energy levels are strongly affected by the electric field gradient, QR transition frequencies are distinct to a given material containing it [5]. Reports of compounds with the same transition frequencies have not been found in the literature.

1.2 QR Detection Challenges

QR detection systems present four challenges that prevent commercialization. The first challenge is that the QR response is inherently small and so, the signal-to-noise ratio (SNR) is small [1]. The low measurement SNR of the QR response requires long detection times in order to increase the probability of detection. The second challenge is the temperature dependence of transition frequencies of the desired target compound. As will be discussed in more detail in Chapter 3, the exact temperature of the target is typically unknown, and therefore, it is difficult to predict the change to the transition frequency during detection. The third challenge is interference from external noise sources. AM broadcast stations or nearby electrical devices are two examples of external noise sources with spectra that can overlap with the QR response. For example, the AM broadcast band spans 550 kHz to 1.6 MHz while the transition frequency for pentaerythritol tetranitrate (PETN) at room temperature is centered at 890 kHz [13]. A radio station broadcasting at this frequency will be the primary RF interference source and produce a signal much

larger than the QR response. The fourth challenge is interference induced by the strong RF pulses required to generate a QR response. Sources of this interference involve the response of materials within the search volume, as well as ringing induced in the receiver probe. This interference leads to missed detections and false alarms.

Recent work at the Space & Intelligence division of Raytheon Technologies has made significant progress in reducing the effect of external noise by developing a QR receiver probe that rejects far field external RF interference by more than 60 dB, without attenuating the near field QR signal [12]. The work in this thesis is aimed at assisting Raytheon in developing a commercial QR sensor based on their receiver probe by focusing on the other three challenges. As will be discussed in Chapter 3, because the project aims to design a broadband receiver, the design will inherently account for the variation in transition frequency due to temperature by searching over a band of frequencies rather than a specific transition frequency. In Chapter 2, this thesis will present a brief overview of QR detection systems and discuss a technique known as phase cycling that is commonly used to eliminate internal noise that QR detection systems are susceptible to. Lastly, the combination of a thoughtful amplifier design and techniques for attenuating the noise will effectively improve the measurement SNR.

1.3 Project Goals

Raytheon's receiver uses a series-parallel matching network that noise matches the probe to a low-noise amplifier to maximize the SNR, as discussed in Chapter 3. However, the matching network introduces two new challenges. The first challenge is an increase in detection time imposed by the need to tune the matching network. The matching network consists of two capacitors that each need to be tuned depending on the transition frequency of the explosive or narcotic of interest, the change to the transition frequency based on the temperature of the search volume and the change to the probe impedance as test material is brought closer to the probe. The second challenge is that the matching network forms a resonant circuit that will ring in response to applied RF pulse [17]. The ringing in the received signal is larger than the QR response and requires increasing the dead time between the end of an RF pulse and the opening of the receiver window to avoid receiving the ring. Therefore, it is highly desirable to build a detection system that is non-resonant or only has a resonant peak outside the bandwidth of detection.

This work in this thesis presents a broadband system without a noise-matching network. The immediate benefits associated with eliminating the matching network are

eliminating the time to tune and the ringing in the received signal while the tradeoff is an increase in noise figure. This thesis will show that the loss of dB in the noise figure is compensated by an increase in the measured QR response. As will be discussed in Chapter 2 and 4, the reduction of ringing in the received signal will decrease the required dead time during pulse sequencing and allows the inductive sensor to receive pulses with a larger amplitude before the signal decays to the noise floor. The additional pulses translate into a larger average QR response to improve the measurement SNR.

This thesis begins by giving an overview of QR detection systems in Chapter 2. This chapter describes the architecture at a high level, introduces RF pulse techniques, and finishes with the limitations of the parameter selection in the RF pulse techniques. Chapter 3 starts by discussing how noise matching the probe to the preamplifier improves measurement SNR. The second section of Chapter 3 discusses the tuned matching network required for noise matching. The last section of Chapter 3 discusses the disadvantages of using a tuned matching network. Chapter 4 first provides an overview of recent broadband, low-noise receiver designs in the fields of magnetic particle imaging (MPI) and magnetic resonance (MR). Next, the broadband prototype is described. Finally, this chapter presents the tradeoffs associated with the broadband design in comparison to the conventional receiver designs with MATLAB simulations and Multisim designs to predict the prototype performance. Chapter 5 provides a brief discussion of the potential of the prototype presented in this thesis. The chapter begins by reviewing the key results discussed in this thesis, followed by a section providing recommendations for future work.

Chapter 2
QR Detection Systems

Section 1.2 introduced the 4 challenges with QR detection. This chapter discusses the QR detection system at a high level before two specific QR detection system designs are discussed in Chapter 3 and Chapter 4. Section 2.1 discusses the architecture of a QR detection system. Section 2.2 introduces a pulse sequence that reduces the thermal noise voltage to improve the receiver SNR and a modification to this sequence that eliminates parasitic responses. Finally, Section 2.3 discusses how pulse parameters affect the amplitude of the QR response and are of importance in Chapter 4.

2.1 Architecture

Figure 2.1 shows a block diagram of a prototype QR detection system that uses a noise-matched receiver. The QR console generates the train of RF pulses and takes the received response and demodulates it to the desired baseband frequency. Typically the baseband frequency is 10 kHz so that the received QR signal appears as an exponentially decaying 10 kHz signal.

The train of RF pulses passes through an RF power amplifier whose 50 Ohm output is matched to the impedance of the transmit (TX) loop. The RF power level is set to produce about 1 Gauss field at the transition frequency across the search volume. The required output power depends on the size of the search volume. It can range from a few hundred watts for a tabletop detector to several kilowatts for a search volume large enough to inspect a vehicle.

At the end of an RF pulse, there is energy stored in the capacitance of the TX matching network and the magnetic field of the transmit loop. An external Q-damping loop is used to quickly dissipate the stored energy. This loop is in series with a damping resistance, $R_{d,TX}$ and an RF switch A. During RF pulse excitation, the RF switch A is

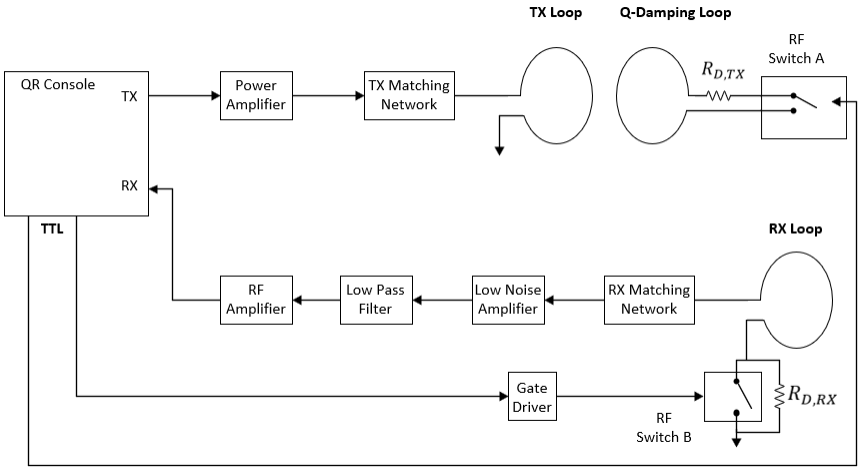

Figure 2.1. QR detection system using matching networks and Q-damping loop.

opened so as not to affect the tuning of the transmit loop. At the end of the RF pulse, switch A is closed for a time interval T_D to dissipate the stored energy in the damping resistance, $R_{d,TX}$.

The QR signal is detected using the receive (RX) loop. This loop is colinear with the TX loop and its physical design is such that it is isolated from the TX loop by 60 dB [12]. Despite this decoupling, there is a considerable signal introduced into the RX loop during transmission. As discussed earlier, the noise matching network and the RX loop formed a resonant circuit with a Q factor typically between 50 and 100, and so the energy coupled to the RX loop during RF pulses takes time to decay at the end of the RF pulse. To increase the decay rate, the RX loop uses a de-Q circuit consisting of an RF switch in parallel with a receiver damping resistance, $R_{d,RX}$. During receive, the RF switch B is closed, placing a dead-short across $R_{d,RX}$ and resulting in a high Q-factor. Immediately after an RF pulse, the RF switch B is opened for a time interval T_D which effectively increases the resistance for the RX loop by $R_{d,RX}$ and decreases the Q factor. The period of reduced Q-factor introduces a dead time, T_D between when the RF pulse ends and when the receiver window opens. Figure 2.2 shows the timing diagram of the transmit pulse, Q-spoiling network, and the opening of the receive window.

Figure 2.3 shows the architecture of the QR console that is responsible for the timing of transmitting RF pulses, receiving the QR signal, and controlling the RX de-Q circuit and the switch to the TX Q-damping loop. Section 2.2 will explain the TX pulse sequence in more detail.

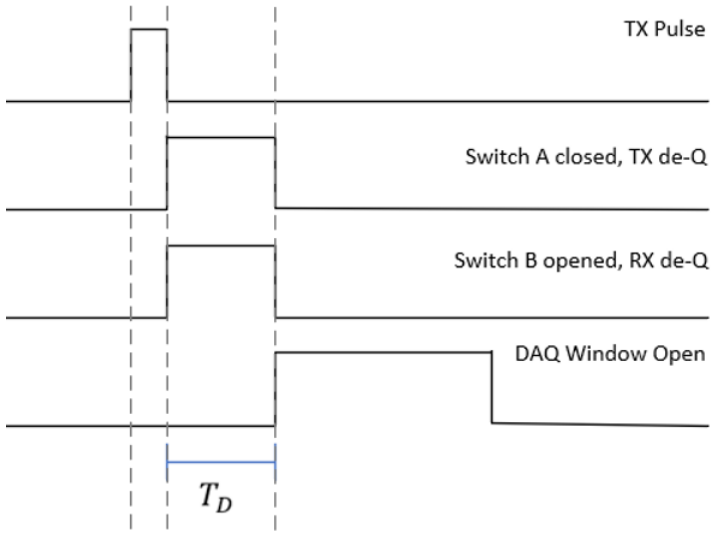

Figure 2.2. The timing sequence of the transmit RF pulse, TX Q-switch, RX Q-switch, and DAQ window.

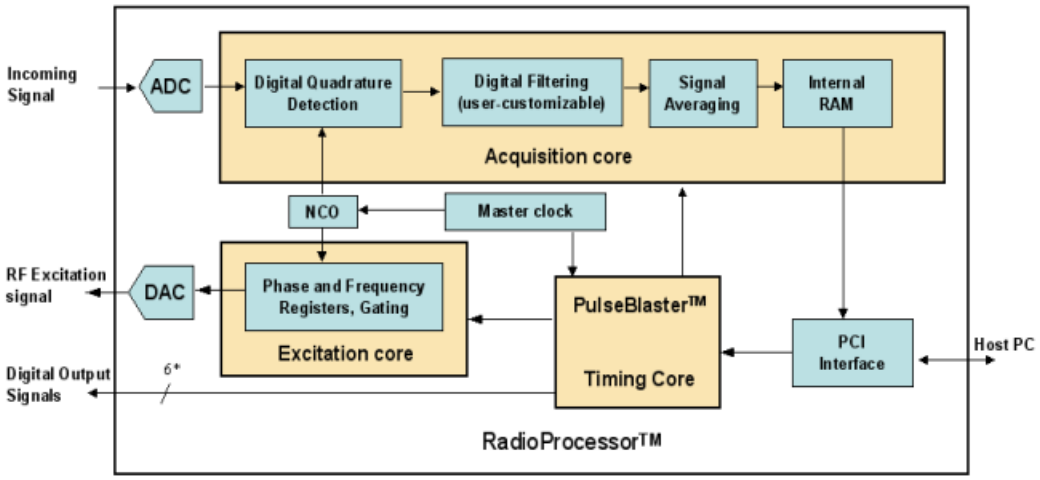

Figure 2.3. The QR console is a SpinCore Technologies Radio Processor.

2.2 Pulse Sequence

In QR detection systems where the search volume is larger than the volume of the target, the amplitude of the QR response to a single RF pulse is on the order of the thermal noise associated with the receiver probe. The thermal noise level can be reduced below the QR signal level using signal averaging [14]. The spin-lock spin-echo (SLSE) sequence produces a train of QR responses that significantly increase the measurement SNR per

unit time through signal averaging [15].

Following each RF pulse is the parasitic transient response to the RF pulse and the QR free induction decay (FID) generated by the RF pulse, which is an exponentially decaying sinusoid with a time constant T_2^*. A spin echo is generated by two RF pulses. The first and second pulses, whose centers are spaced by the time interval, $T_E/2$, each generate an FID following the RF pulse. The second pulse re-phases the nuclei from the first RF pulse and forms a spin-echo that is centered at T_E, where T_E denotes the time-to-echo.

The spin-echo resembles two back-to-back FIDs that are centered at $T_E/2$ from the second RF pulse. As $T_E/2$ is typically larger than the time constant of the ringdown due to RF pulses and transient in the RF receiver gate, these parasitic responses have a smaller effect on the measurement of the spin-echo. The peak amplitude of the spin-echo is smaller than that of the FID due to the process known as spin-spin relaxation, which has a time constant, T_2. It can be shown that a spin-echo is represented by [18]

$$s_{se}(t) = Ae^{\frac{-T_E}{T_2}} e^{\frac{-|t-T_E|}{T_2^*}} \cos(\omega_* t), \tag{2.1}$$

where A is the peak amplitude of the FID response and ω_* is the QR transition frequency.

It can be shown that the Fourier transform of the spin-echo response, $s_{se}(t)$ has the Lorentzian line-shape [18]

$$|S_{spinecho}(j\omega)| = \frac{A\omega_* T_2^* e^{\frac{-T_E}{T_2}}}{1 + T_2^{*2}(\omega - \omega_*)^2}. \tag{2.2}$$

In the frequency domain, the full-width half-maximum (FWHM) of the line shape is $1/(2T_2^*)$ Hz. For most materials, the FWHM is on the order of 1 kHz.

The SLSE sequence generates a series of spin echo responses by appending additional re-phasing pulses to the spin echo sequence discussed above. Successive echoes are averaged together to increase the measurement SNR. The peak amplitude of successive spin-echoes relaxes with an effective spin-spin relation time constant $T_{2,eff}$. Marino made a significant observation in that [15]

$$T_{2,eff} \propto \frac{1}{T_E^5}. \tag{2.3}$$

As a result, by reducing the pulse spacing T_E, the peak amplitude of successive echoes decays at a slower rate, increasing the measurement SNR of the average response of the SLSE sequence.

While averaging successive spin echoes in the SLSE response reduces the level of noise, it does not eliminate the whole transient response from ringing caused by RF excitation and transient caused by switching RF gates in the receiver. A technique known as phase-cycling can reduce these parasitic responses without reducing the average spin-echo signal, at the expense of also eliminating the QR FID signal following each re-phasing pulse. The phase-cycled SLSE sequence consists of two separate SLSE signals separated by a delay of time, T_d. These two sequences differ by the phase of the RF lock pulses. By setting the phase difference between them to 180 degrees, the spin echoes generated in the first sequence are 180 degrees out of phase with the spin echoes in the second sequence. As both sequences use the same phase for re-phase pulses, the QR FID signal and parasitic noise generated after re-phasing in both sequences are in phase. And so, by subtracting the response of the second sequence from the first, the spin echoes will add while the QR FID and the parasitic signal subtract. The elimination of the parasitic response using phase cycling requires that the receiver chain is not saturated.

The successive spin echo sequences must be separated by a time delay, T_d, that is greater than the spin-lattice relaxation time T_1 so the nuclei are in thermal equilibrium before the next lock pulse [18]. The number of spin echoes to be averaged, N_{avg} is determined by the number of spin echo sequences, N_s, and the number of echoes contained in a single sequence, N_e. Increasing N_{avg} allows a larger number of spin echos to be averaged and increases the SNR of the average spin-echo by $\sqrt{N_{avg}}$. However, there is a limit to the increase in SNR that will be discussed in Section 2.3.

Although phase cycling the SLSE sequence reduces the parasitic transient response and the QR FID significantly, Q-spoiling the receiver and transmit loops is still required as the energy stored by the RX is large and typically saturates the receiver. Figure 2.4 shows the phase-cycle sequence. The notation $(\theta)_\phi$ indicates the angle, θ the nuclei rotate and the phase, ϕ of the RF pulse.

Each RF pulse causes the nuclei to rotate at the angle that depends on both the peak amplitude of the RF pulse B_1, as well as the pulse width t_w. Selection of the pulse sequence parameters, B_1, t_w, T_E, N_e, N_s, T_D, and T_d are discussed in the next section.

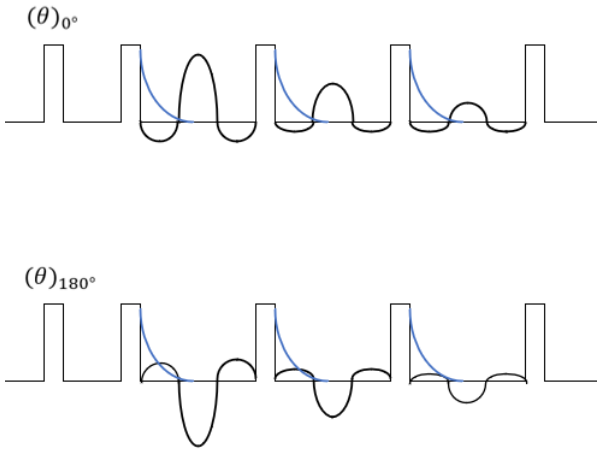

Figure 2.4. The spin-lock spin-echo sequence with phase cycling.

2.3 Pulse Parameter Selection

Choosing pulse parameters for the phase-cycled sequence presents a tradeoff between increasing the measurement SNR by increasing the number of average echoes

$$N_{avg} = N_s N_e \tag{2.4}$$

and the detection time

$$T_{det} = N_s(N_e T_E + T_d). \tag{2.5}$$

The rationale for choosing the pulse parameters is now discussed in the following order: the time delay between successive sequences T_d, the pulse amplitude B_1, the pulse width t_w, the number of sequences N_s, the number of echoes per sequence N_e, the time-to-echo T_E, the dead time T_D.

The time delay, T_d between successive spin echo sequences is chosen so a new spin echo sequence does not begin before the nuclei return to thermal equilibrium while also avoiding a long detection time. When in the thermal equilibrium state, the nuclei will produce the largest possible QR response when excited. While choosing T_d much larger than T_1 ensures the largest possible QR signal, it also increases T_{det}. Typically, the value of T_d is set equal to T_1.

The application of an RF pulse, whose frequency matches the QR transition frequency,

causes the nuclei to rotate by an angle

$$\theta = \gamma B_1 t_w, \tag{2.6}$$

where t_w is the pulse width, B_1 is the peak value of the applied RF pulse, and γ is the gyromagnetic ratio associated with the nuclei to be detected. Ideally, in the SLSE pulse sequence, the value of θ is chosen to maximize the amplitude of the FID after the lock pulse. The amplitude of the FID is proportional to $j_1(\theta)$, where $j_1(\theta)$ is a spherical Bezel function of the first kind of order one that is maximized when $\theta = 0.66\ \pi$ [18].

As shown in Eq. (2.6), B_1 and t_w are inversely related. Ideally, the pulse width is small for 2 reasons. First, the bandwidth of the RF pulse is inversely proportional to t_w. It is important that the pulse width is sufficiently small so that the spectrum of the RF pulse overlaps the Lorentzian line shape of the QR transition. This is important because there is uncertainty in the QR transition frequency where the temperature of the target material is not known precisely. Second, the pulse width adds to the time-to-echo, T_E. By increasing the pulse width, the time-to-echo increases and effectively decreases $T_{2,eff}$, which in turn, reduces the measurement SNR.

However, B_1 should also be small in order to reduce the cost of the power amplifier and components in the TX matching loop and Q-spoil switches. As the detection volume increases, so must the power applied by the RF power amplifier to achieve a given value of magnitude. For example, 100 watts is sufficient to produce a 1 Gauss field in the search volume associated with a tabletop scanner. On the other hand, to achieve a 1 Gauss field in a volume large enough to contain a car, a 10 kW power amplifier is needed.

Typically, B_1 is about 1 Gauss and the pulse width is around 1 ms. As an example, consider the detection of ammonium nitrate using an applied magnetic field of $B_1 =$ 1 Gauss. For ammonium nitrate, the detected nuclei is nitrogen-14, where γ is 1943 (rad/sec)/Gauss. In this case, the value of t_w is approximately 1.067 ms which yields θ $= 0.66\pi$.

The number of echoes in a sequence, N_e is chosen to maximize the measurement SNR of the average signal. While increasing the value of N_e will decrease the noise floor, it also decreases the signal amplitude due to the peak amplitude of the spin echoes decaying as $T_{2,eff}$. For this reason, T_E and N_e are chosen so that

$$N_e T_E < 3T_{2,eff}. \tag{2.7}$$

The value of N_E is chosen using Eq. (2.7) after the value of T_E is chosen as discussed at

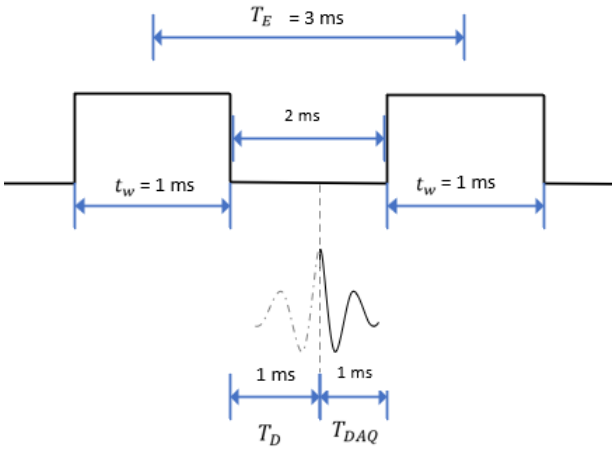

Figure 2.5. The timing of a single spin-echo for a system with a resonant circuit and dead time of 1 ms.

the end of the section. The number of spin echo sequences, N_s, is typically chosen as $N_2 = 2$, to avoid increasing detection time as the delay, T_d between N sequences is T_1.

Limitations can be placed on the time-to-echo based on the inverse-linewidth parameter, T_2^*, and the effective spin-spin relaxation time constant, $T_{2,eff}$. Reducing the time-to-echo will maximize $T_{2,eff}$ as more QR responses will be generated per unit time for signal averaging as shown in Eq. (2.3). However, since the spin-echos are centered at T_E seconds after an RF pulse, the time-to-echo must be larger than T_2^* to ensure the QR responses do not destructively interfere. Since the inverse-linewidth parameter and the effective spin-spin relaxation time constant are unknown prior to detection, they must be estimated to determine a time-to-echo for the pulse sequence.

It is desirable to choose the smallest value of T_E that satisfies

$$T_E \geq t_w + T_D + T_{DAQ}. \tag{2.8}$$

Figure 2.5 shows the typical timing of a spin-echo for a system with a resonant matching network as described in Section 2.1 where the time-to-echo is the sum of the entire RF pulse width, the dead time, and the DAQ window, T_{DAQ}.

As described earlier in this section, t_w is typically 1 ms. The minimum value T_{DAQ} is typically 1 ms so that several cycles of the QR baseband signal can be observed. The dead time, T_D, is needed to remove undesirable ringing using a Q-spoil circuit. In a system with a noise matching network, the dead time is typically 1 ms which yields $T_E = 3$ ms.

Decreasing t_w, T_D, or T_{DAQ} will decrease T_E, and as shown in Eq. (2.3), will increase the decay rate of the spin echo envelopes, $T_{2,eff}$. As discussed earlier, an increase in the peak amplitude of the average spin-echo increases the measurement SNR. Therefore, it is desirable to design a receiver that does have a resonant circuit. Chapter 3 and Chapter 4 will use the impact of dead time to compare a design that forms a resonant circuit to a design that does not form a resonant circuit.

Chapter 3
Series-Parallel Matching Design

This chapter presents the conventional method of receiver design. Section 3.1 characterizes the probe and amplifier network and then derives the required input impedance to the amplifier network to achieve the smallest noise factor. Section 3.2 demonstrates the parallel-series matching approach that when inserted between the probe and the preamplifier, transforms the probe impedance to match the ideal input impedance presented in Section 3.1. Finally, Section 3.3 discusses the disadvantages of this matching network design which introduces the need for the broadband design presented in Chapter 4.

3.1 Noise Matching

This section considers the signal-to-noise ratio of quadrupole resonance measurements and in particular, the effect of the thermal noise of the probe resistance and the noise contributed by the RF amplifier. This analysis does not consider external sources of noise such as atmospheric noise due to electrical systems and RF interference from amplitude modulation (AM) broadband systems or nearby electrical appliances.

Figure 3.1 shows a simplified electrical model of the probe used to detect QR signals. The self-inductance of the probe is L_p. The self-resistance due to the wire is R_p and is larger than the DC resistance of the wire due to skin depth. The signal, V_s represents the source voltage of the QR response. Associated with the real resistance, R_p is a thermal noise voltage, V_p, due to the random motion of electrons in the probe. The root-mean-square (RMS) thermal voltage is

$$v_{p,rms} = \sqrt{4KTR_p\Delta B}, \qquad [V] \tag{3.1}$$

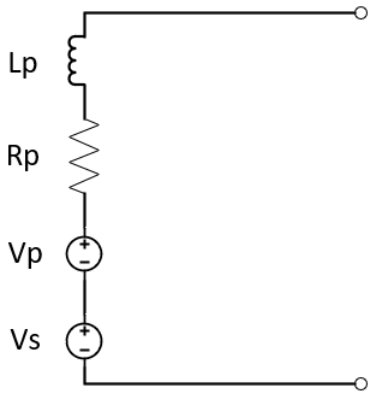

Figure 3.1. The probe model including thermal noise source associated with self-resistance.

in terms of the real resistance of the probe R_p, Boltzmann's constant K (1.38E-23 W*s/K), the measurement bandwidth ΔB in Hertz, and the temperature T in Kelvin [19]. For convenience, ΔB is typically set to 1 Hz, and v_p is reported in units of volts, RMS per square root of hertz as given in Eq. (3.2). This value can be scaled by the measurement bandwidth ΔB to achieve the measured value as

$$v_{p,rms} = \sqrt{4KTR_p} \qquad \left[\frac{V}{\sqrt{Hz}}\right]. \tag{3.2}$$

Suppose that the probe is connected to a noiseless amplifier with an input resistance of R_i as shown in Figure 3.2. The SNR at the amplifier input, SNR_i, is the ratio of signal power to noise power,

$$SNR_i = \frac{v_{s,rms}^2 \frac{(\frac{R_i}{R_1+R_p})^2}{R_i}}{v_{p,rms}^2 \frac{(\frac{R_i}{R_1+R_p})^2}{R_i}}, \tag{3.3}$$

where the signal source is v_s and the noise source is v_p [16]. The source voltage across R_i is the voltage, v_s, scaled by the voltage division between the series resistors R_p and R_i. Similarly, the noise voltage across R_i is the voltage, v_p, scaled by the voltage division of the series resistors once more. The SNR_i simplifies to

$$SNR_i = \frac{v_{s,rms}^2}{v_{p,rms}^2}. \tag{3.4}$$

The amplifier shown in Figure 3.2 is greatly oversimplified and does not show the electric noise introduced by the amplifier's components. Due to the electric noise, the

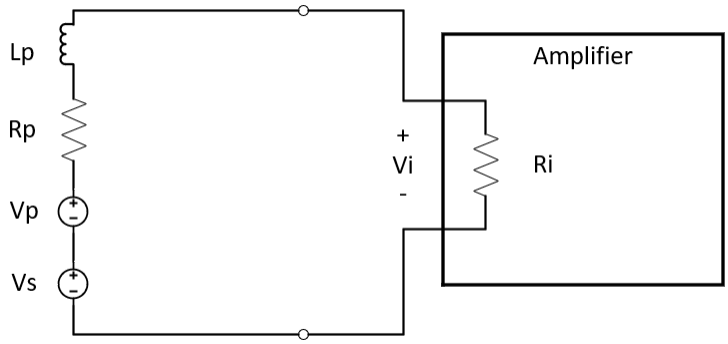

Figure 3.2. Probe connected to the input of a noiseless amplifier with internal resistance.

SNR at the output of the amplifier, SNR_o must be smaller than SNR_i. The noise factor is defined as

$$F = \frac{SNR_i}{SNR_o}, \tag{3.5}$$

and is a figure of merit for the amplifier. Just as SNR_o must be smaller than SNR_i, the noise factor cannot be less than 1 because this would mean that the electric noise of the amplifier eliminated the input noise, which is impossible. Therefore, it is desirable to achieve a noise factor as close to 1 as possible.

The noise factor converted from a linear measurement, which is unitless, to units of dB, is the noise figure defined as

$$NF = 10 \log_{10}(F). \tag{3.6}$$

The factor of 10 reflects that the ratio of SNR, given as the noise factor, is in terms of power instead of voltage. For a noiseless amplifier, the noise figure is 0 dB. In practice, common low-noise amplifiers have a noise figure of about 0.3 dB.

It turns out that the noise figure is dependent on the impedance of the source as shown in the following analysis. Figure 3.3 shows a more detailed model in phasor notation of the amplifier connected to the probe.

The noise contributions from the amplifier are represented by a voltage source, e_n, and a current source, i_n as shown in Figure 3.3 [16]. As with the thermal noise voltage of the probe, it is convenient to express the amplitude of these sources over a 1 Hz bandwidth. And so, the units of e_n and i_n are $\mathrm{V}/\sqrt{(Hz)}$ and $\mathrm{A}/\sqrt{(Hz)}$ respectively. Using Thevenin's theorem, the circuit shown in Figure 3.3 is reconfigured so that all thermal noise is represented by an equivalent input noise voltage, $\tilde{V}_{ni}$, as shown in Figure

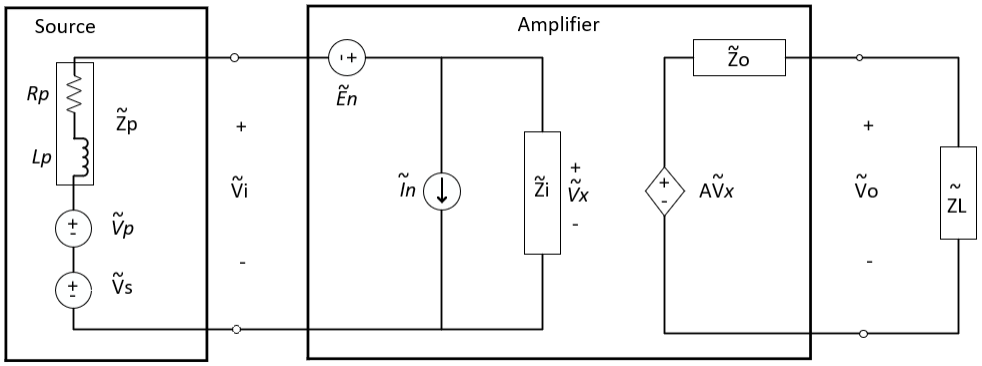

Figure 3.3. The probe connected to an amplifier network with the noise modeled by voltage and current sources.

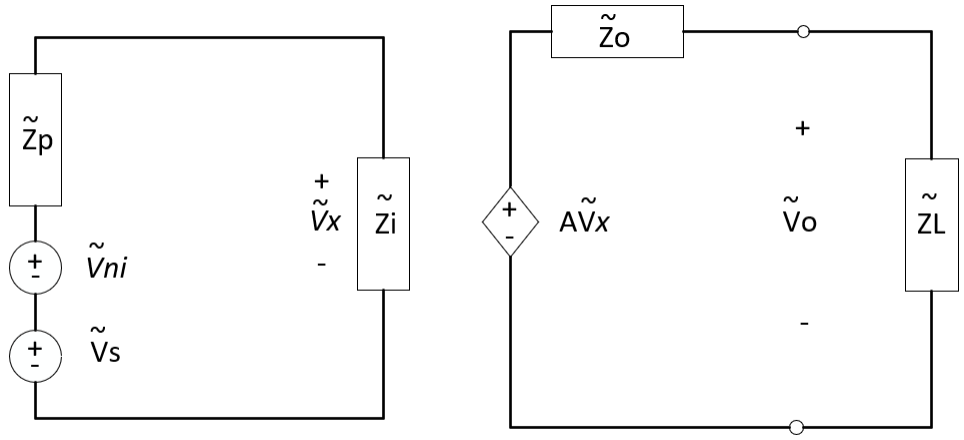

Figure 3.4. The Thevenin equivalent circuit of combining the amplifier noise sources and the signal noise into a single voltage source.

3.4. It can be shown that the noise sources $\tilde{E}_n$, $\tilde{I}_n$ and $\tilde{V}_p$ can be represented by [17]

$$\tilde{V}_{ni} = \tilde{V}_p + \tilde{E}_n + \tilde{Z}_p \tilde{I}_n. \tag{3.7}$$

Recall the input signal-to-noise ratio of the amplifier as given in Eq. (3.4). The output signal-to-noise ratio of the amplifier includes the noise of the amplifier, $\tilde{V}_{ni}$. The analysis of the noise factor for the circuit in Figure 3.4 is done in the time domain. Using the simplified circuit, the noise factor is

$$F = \frac{SNR_i}{SNR_o} = \frac{(\frac{v^2_{s,rms}}{v^2_{p,rms}})}{(\frac{v^2_{p,rms}}{v^2_{ni,rms}})} = \frac{v^2_{ni,rms}}{v^2_{p,rms}}, \tag{3.8}$$

where v_{ni} is the RMS of the input noise voltage, and v_p is the RMS of the thermal noise voltage [17]. A few assumptions need to be made to complete the analysis using RMS values of the voltage sources [16]. First, assume the noise processes are ergodic for electronic circuits so that the squared RMS value for a voltage source is

$$v_{rms}^2 = E\{\tilde{V}\tilde{V}^*\} = \overline{\tilde{V}\tilde{V}^*}, \tag{3.9}$$

where E is the expected value and the voltage source value is in the phasor domain. The squared RMS of the thermal noise voltage given in Eq. (3.2) is

$$v_{p,rms} = 4KTR_p \left[\frac{V}{\sqrt{Hz}}\right]. \tag{3.10}$$

To solve for the squared RMS value of the input voltage, $\tilde{V}_{ni}$ as defined in Eq. (3.7) is substituted into the RMS equation to obtain

$$v_{ni,rms}^2 = E\{\tilde{V}_{ni}\tilde{V}_{ni}^*\} = E\{(\tilde{V}_p + \tilde{E}_n + \tilde{Z}_p\tilde{I}_n)(\tilde{V}_p + \tilde{E}_n + \tilde{Z}_p\tilde{I}_n)^*\}. \tag{3.11}$$

The second assumption is that the sources $\tilde{V}_{ni}$, $\tilde{E}_n$, and $\tilde{I}_n$ are independently and identically distributed so the correlation between any combination of these sources is zero [16]. The third assumption is that the sources $\tilde{V}_{ni}$, $\tilde{E}_n$, and $\tilde{I}_n$ are zero mean processes [16]. Using these two assumptions, the squared RMS value of the input voltage is

$$v_{ni,rms}^2 = 4KTR_p + e_{n,rms}^2 + i_{n,rms}^2(R_p^2 + \omega^2 L_p^2). \tag{3.12}$$

Note that the value of $v_{ni,rms}^2$ is dependent on the real resistance and reactance of the probe, the voltage and current noise sources of the amplifier, and the detection frequency, ω. Substituting the squared RMS value of the input noise voltage to the amplifier and the squared RMS value of the thermal noise voltage into the noise factor equation given in Eq. (3.8) yields the noise factor for the amplifier

$$F = \frac{4KTR_p + e_{n,rms}^2 + i_{n,rms}^2(R_p^2 + \omega^2 L_p^2)}{4KTR_p}. \tag{3.13}$$

To maximize the SNR at the output of the amplifier, it is necessary to make the noise factor as close as possible to unity. As the value of e_n and i_n are fixed for a given amplifier, this is accomplished by appropriately choosing the values of L_p and R_p. the

values of L_p and R_p that minimize F must satisfy $\partial F/\partial L_p = 0$ and $\partial F/\partial R_p = 0$. Using Eq. (3.13),

$$\frac{\partial F}{\partial L_p} = \frac{2L_p\omega^2 i_{n,rms}^2}{4KTR_p} = 0 \; for \; L_p \; = \; 0. \tag{3.14}$$

Similarly,

$$\frac{\partial F}{\partial R_p} = \left(\frac{1}{4KTR_p^2}\right)\left(-e_{n,rms}^2 + R_p^2 i_{n,rms}^2 - i_{n,rms}^2\omega^2 L_p^2\right). \tag{3.15}$$

Since L_p must be 0, Eq. (3.15) is set to 0 and solved for the probe resistance, R_{opt} that optimizes noise factor [16]. Setting $\partial F/\partial R_p = 0$ using Eq. (3.15) yields

$$R_{opt} = \frac{e_n}{i_n}. \tag{3.16}$$

Most commercial low-noise preamplifiers are designed so that the source impedance that minimizes the noise figure is 50 Ω, which is denoted as R_o. And so, to achieve a minimum noise figure, it is necessary to transform the source impedance to R_o. Choosing the source impedance to minimize the noise figure is called noise matching. The conclusion in Eq. (3.14) poses a design issue because the probe reactance cannot be minimized to 0. Section 3.2 will discuss minimizing the noise factor of the amplifier by using a series-parallel matching network to simultaneously transform the probe reactance to 0 and the probe resistance to R_{opt}.

3.2 Matching Network

Section 3.1 showed that the noise factor of the amplifier is minimized when the probe impedance looking into the amplifier is equal to R_{opt}. This section will show that matching networks can transform reactive loads into purely restive loads as desired [20].

A series-parallel capacitive matching network is shown in Figure 3.5 where the source is the equivalent model for the receiver probe, C_p is the parallel capacitor of the matching network, C_s is the series capacitor of the matching network, and Z_{in} is the impedance looking into the matching network. The value of C_s and C_p are chosen so that the impedance looking into the probe is

$$Z_o = R_{opt} + j0 \; \Omega \tag{3.17}$$

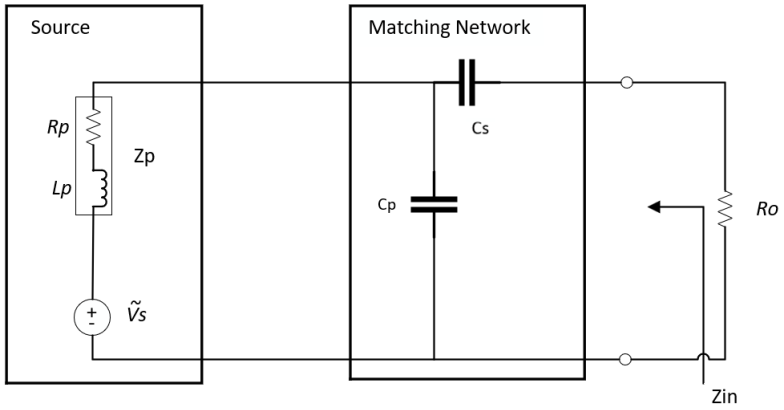

Figure 3.5. Parallel-Series Matching Network

at an operating frequency, ω_o [16].

The following analysis derives the values of C_p and C_s to achieve the desired impedance transformation. The impedance looking into the matching network from the amplifier, Z_{in} is derived from the first principles as

$$Z_{in}(j\omega) = -j\frac{1}{\omega C_s} + \frac{(j\omega L_p + R_p)(1 - \omega^2 L_p C_p - j\omega R_p C_p)}{(1 - \omega^2 L_p C_p)^2 + (\omega R_p C_p)^2}. \tag{3.18}$$

Equivalently, Z_{in} is considered as the output impedance of the matching network after transforming the source impedance, Z_p. The impedance, Z_{in} is rearranged into the real component,

$$Re\{Z_{in}(j\omega)\} = \frac{R_p}{(1 - \omega^2 L_p C_p)^2 + (\omega R_p C_p)^2}, \tag{3.19}$$

and the imaginary component,

$$Im\{Z_{in}(j\omega)\} = \frac{\omega L_p(1 - \omega^2 L_p C_p)}{(1 - \omega^2 L_p C_p)^2 + (\omega R_p C_p)^2} - \frac{1}{\omega C_s}. \tag{3.20}$$

In order to minimize the noise figure, the values of C_p and C_s must be chosen so that

$$Re\{Z_{in}(j\omega_o)\} = R_o, \tag{3.21}$$

and

$$Im\{Z_{in}(j\omega_o)\} = 0, \tag{3.22}$$

at the desired operating frequency. After setting Eq. (3.19) equal to R_o, C_p will have two possible roots,

$$C_p = \frac{L_p}{\omega_o^2 L_p^2 + R_p^2} \pm \sqrt{\left(\frac{L_p}{\omega_o^2 L_p^2 + R_p^2}\right)^2 - \frac{1 - \frac{R_p}{R_o}}{\omega_o^4 L_p^2 + \omega_o^2 R_p^2}}, \tag{3.23}$$

in which the viable root is determined by solving for the series capacitance, C_s. The imaginary term of the output impedance given in Eq. (3.20) is set equal to 0 and solved for C_s to obtain,

$$C_s = \frac{R_p}{R_o}\left(\frac{1}{\omega_o^2 L_p(1 - \omega_o^2 L_p C_p - R_p C_p \frac{R_p}{L_p})}\right). \tag{3.24}$$

Based on the fundamental principle of minimum energy, Eq. (3.23) and Eq. (3.24) are constrained to positive capacitor and inductor values [16]. For C_s to be positive, C_p must satisfy

$$C_p < \frac{1}{\omega_o^2 L_p^2 + R_p^2/L_p}. \tag{3.25}$$

Given this constraint on C_p, the only valid root is

$$C_p = \frac{L_p}{\omega_o^2 L_p^2 + R_p^2} - \sqrt{\left(\frac{L_p}{\omega_o^2 L_p^2 + R_p^2}\right)^2 - \frac{1 - \frac{R_p}{R_o}}{\omega_o^4 L_p^2 + \omega_o^2 R_p^2}}. \tag{3.26}$$

As the value of C_p must be positive, Eq. (3.26) requires that $R_o > R_p$. This constraint is reasonable since the receiver probe resistance is typically less than one ohm.

Using the values of C_p and C_s given by equations (3.24) and (3.26) respectively, noise matches the NQR probe to the low-noise preamplifier. However, C_p and C_s depend on R_p, L_p, and ω. As briefly discussed in Section 1.2, the frequency of detection changes per material of interest and temperature of the material while the resistance and reactance of the receiver probe changes based on the material in the search volume. Therefore, the values of C_p and C_s must be tuned to maintain noise matching, despite changes in the material or source resistance. Section 3.3 will discuss this challenge in more detail.

3.3 Disadvantages

A practical QR detection system must be capable of detecting several different explosives each with a resonant frequency centered in the range of 400 kHz to 4MHz. For example, pentaerythritol tetranitrate (PETN) is detected at 890 kHz while C-4 is detected at 3.410 MHz. Using a single probe coil requires changing C_p and C_s to tune for different targets.

Another challenge is that conductive materials placed within the search volume can inductively couple to the receiver probe coil, and as a result, change the values of L_p and R_p looking into the probe. This interference also requires re-tuning C_s and C_p so that the probe remains noise matched to the preamplifier. Because of this, it is not possible to rely on a loop-up table to choose the value of C_p and C_s for a given target. The process of re-tuning C_s and C_p increase the detection time.

The matching network formed by C_p and C_s forms a tuned circuit at the QR transition frequency. As the resistance of the probe coil is small, this resonant circuit possesses a relatively high Q-factor, on the order of 100. This presents two challenges as described below. First, it introduces a dead time in the receiver that increases T_E. As discussed in Section 2.3, this decreases the measurement SNR. Second, the high Q-factor results in a narrow bandwidth, which will result in missed detections if there is an offset between the turned frequency of the probe coil and the QR transition frequency due to uncertainty in the temperature of the material.

Although the transmit and receive loops shown in Figure 2.1 are designed to be uncoupled, a small amount of energy during RF pulse excitation is coupled into the tuned receiver probe. Because of the high Q-factor of the tuned receiver probe, following the RF pulse, there is a large exponentially decaying response at the output of the matching network. As this voltage is large enough to saturate the preamplifier, phase-cycling discussed in Section 2.2 did not reduce the ringing. Instead, a Q-spoil circuit is included in the receiver loop as discussed in Section 2.1. While the Q-spoil is switched to reduce the ringdown, it introduces a dead time, T_D. As discussed in Chapter 2, the dead time will only decrease the measurement SNR by decreasing $T_{2,eff}$.

It is well known that QR transition frequencies are temperature sensitive as much as 1 kHz/C° [21]. For example, Table 3.1 shows the potassium -39 QR transition frequency in potassium chlorate, a substitute for ammonium nitrate in improvised explosive devices, as a function of temperature [22]. From this table, a 20 F°change in temperature results in an 11 kHz shift in the transition frequency.

If the matching network is tuned to 531.5 kHz and has a loaded Q-factor, Q_L of 100,

Temp F°	**Temp C°**	ν_*
95°	35°	522.7 kHz
75.2°	24°	531.5 kHz
50°	10°	542.7 kHz

Table 3.1. QR Transition frequencies of potassium -39 at temperatures that are hot, room temperature, or cold to show how the transition frequency could change if the material is outside on a cold or hot day or inside at room temperature.

the corresponding 3 dB bandwidth of the probe is

$$BW_{3dB} = \frac{\nu_*}{Q_L} = \frac{531.5 \text{ kHz}}{100} = 5.315 \text{ kHz}. \tag{3.27}$$

And so a 20 F°uncertainty in temperature will place the QR transition outside of the 3 dB bandwidth of the tuned probe. The 3 dB bandwidth is important because as the signal decreases by 3 dB, the noise needs to be reduced by 3 dB. Section 2.3 explains that the SNR increases by a factor of $\sqrt{N_{avg}}$ and Eq. 2.5 shows that the detection time, T_{det} is linearly proportional to N_{avg}. Therefore, in order to reduce the noise by 3 dB, detection time would need to double, which is unrealistic for a practical detection system.

Chapter 4 presents a broadband design that mitigates each of the challenges listed in this section. Unlike the matching network, the broadband approach presented in Chapter 4 does not have a matching network, nor creates a resonant peak within the bandwidth of detection frequencies which will allow for a smaller dead time and a larger $T_{2,eff}$. Without a matching network, the broadband network significantly decreases detection time by eliminating the time to tune. Lastly, although QR transition frequencies are temperature dependent, a non-tuned, broadband network inherently is capable of detecting within a range of the expected transition frequencies.

Chapter 4
Broadband Receiver Design

Although the matching network method described in Chapter 3 provides a receiver network with a low noise factor, the long tuning time and ringing in the probe prevent the matching network from becoming a commercialized QR detection system. This chapter presents a prototype design of a broadband detection system that does not use a noise-matching network but instead, uses a step-up transformer and a 2-stage preamplifier consisting of low-noise amplifiers in parallel. First, this chapter gives a brief overview of the design parameters and the derivation of the noise factor (F) equation in terms of these parameters. Next, the selection of the design parameter values is discussed. Lastly, the tradeoffs of this design are shared and supported by Matlab and Multisim simulations.

4.1 Overview

This section provides background on non-tuning amplifier network designs presented in areas of research closely related to NQR. The first subsection discusses three areas of research and chooses one design to build upon based on the possible application to a QR detection system. The second subsection derives the noise factor equation of the design selected in the first subsection.

4.1.1 Literature Survey

This subsection discusses three areas of research to produce an amplifier network that does not require tuning. The first area of research is non-foster tuning. The second area of research used a step-up transformer and a low-noise junction-gate field-effect transistor (JFET). The last area of research used a step-up transformer and a 2 stage amplifier

network consisting of parallel operational amplifiers (op amps).

Non-foster tuning is a non-tuning technique in which an active network is used to eliminate the reactance of the probe impedance over a reasonable bandwidth. The active network is a negative impedance converter (NIC) where the impedance looking into the network is

$$Z_{in}(j\omega) = R_p + j0\Omega \tag{4.1}$$

for any frequency, ω in the bandwidth [23]. This technique is commonly used in matching antennas but only has small applications in QR due to the impact on noise figure that is crucial to applications such as QR detection systems [24]. In a comprehensive report of nuclear magnetic resonance (NMR) spectroscopy techniques, Davoodi et al. [24] explains that the NIC uses active components with high levels of noise, unlike the passive components shown in Section 3.2 that typically only contribute thermal noise relative to their resistance. Another concern with non-foster tuning for QR systems is the stability of the matching network. If the magnitude of the NIC is ever greater than the reactance of the coil, the system will go unstable and oscillate [24]. Since a QR system has parasitic responses as described in Chapter 1, the system cannot be assumed stable [23]. Lastly, the non-foster circuit is not a noise-matching network and therefore, would require a transformer to noise match the output impedance of the NIC, which is just the resistance of the probe, to the preamplifier, R_{opt}. As mentioned in Section 3.1, most commercial amplifiers have an R_{opt} of 50 Ohms while an inductive sensor has a resistance of less than 2 Ohms. The transformer required for noise matching, in this case, would have a high turns ratio and become frequency dependent which is ineffective for a broadband design.

The second non-tuning amplifier network consists of a step-up transformer and a carefully chosen low-noise JFET. Mandal et al. [17] describes this design application for an MR system to detect frequencies from 100 kHz up to 3 MHz. Unlike non-foster tuning and the noise matching network of Chapter 3, this design does not eliminate the reactive component of the probe impedance. Instead, a step-up transformer with a turns ratio, N_t, increases the input SNR to the JFET which in turn, decreases the noise factor of the amplifier network [17]. The tradeoff is an input impedance with a high reactive component at high frequencies which risks limiting the network's bandwidth [17]. In addition, due to the high Q-factor of the coil in this experiment, Mandal implemented capacitive feedback at the input of the JFET to dampen any ringing in the transient response [17]. Mandal's design uses the BF862, silicone JFET for the amplifier network

because it has an ultra-low input voltage noise, e_n of 0.8 nV/$\sqrt{Hz}$ and a low input current noise, i_n of 18 fA/$\sqrt{Hz}$, which is far lower than its competitors [27]. However, it is no longer produced and the other JFETs that are similar, do not perform as well.

The final non-tuning network also uses a step-up transformer of turns ratio, N_t, like Mandal's MR design. However, instead of a JFET, the preamplifier is a two-stage network with the first stage of N_p op amps placed in parallel that are then summed in the second stage op amp. Zheng et al. [26] presented this design application to improve the noise performance of a magnetic particle imaging (MPI) system. The range of frequencies used in MPI is relatively low (20 kHz to 1 MHz) in comparison to NQR, however, this does not mean the higher NQR transition frequencies in the range of several MHz are unattainable [26]. The op amps are chosen to have low input current and voltage noise. Since the op amps are in parallel, the gain of the amplifiers will be summed to a total gain, G_{tot} while the effective voltage noise is [26]

$$e_{n,tot} = \frac{e_n}{\sqrt{N_p}}, \tag{4.2}$$

and the effective current noise is

$$i_{n,tot} = \sqrt{N_p} i_n. \tag{4.3}$$

Op amps with a low input current noise are common and so, despite $i_{n,tot}$ increasing with the addition of each op amp in the first stage, the equivalent input current noise will remain low [27]. The method of using operational amplifiers in parallel is more realistic in comparison to finding an ultra-low noise JFET such as the BF862. As mentioned in Chapter 1, this thesis aims to present a viable prototype design for Raytheon Technologies. Therefore, ease of production and access to products must be taken into consideration. Since the BF862 is already a unique JFET and is now, no longer produced, the method of a single JFET used in the amplifier network is not feasible.

This chapter will continue with the method of a step-up transformer and an amplifier network consisting of multiple LNAs in parallel. Given a turns ratio of, N_t, and N_p parallel LNAs, Section 4.1.2 shows that the noise factor for a 1 kHz bandwidth is

$$F = 1 + \frac{\frac{e_n^2}{N_t^2 N_p} + i_n^2 |Z_p^2| N_t^2 N_p}{4KTR_p}. \tag{4.4}$$

4.1.2 Key Result Derivation

Figure 4.1 shows a conceptual diagram of a broadband preamplifier with an input transformer and N_p preamplifiers connected in parallel. Section 4.2 discusses the simulation model based on Figure 4.1.

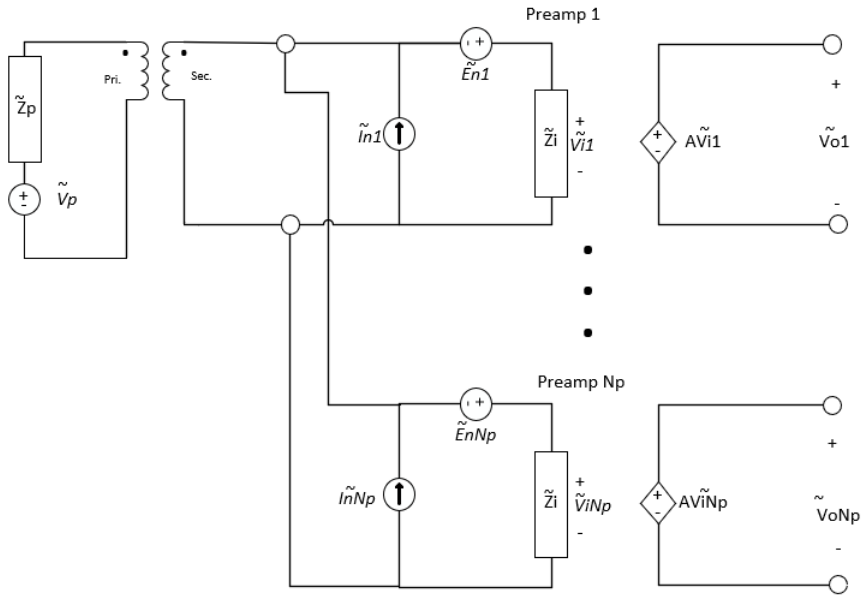

Figure 4.1. Broadband amplifier with input transformer and N_p preamps connected in parallel.

To begin, the transformer is assumed to be a transmission-line transformer with a turns ratio, N_t in which the transformer is ideal and neglects noise sources associated with the transformer. The resulting equivalent model is given in Figure 4.2.

Recall from Chapter 3 that noise factor of an amplifier network is

$$F = \frac{v_{o,rms}^2 \big|_{\text{ due to all noise sources}}}{v_{o,rms}^2 \big|_{\text{ due to } v_p \text{ of the coil}}} \tag{4.5}$$

where $v_{o,rms}$ is the RMS of the total output voltage, $\tilde{V}_o$

$$\tilde{V}_o = \sum_{k=1}^{N_p} \tilde{V}_{o,k} \tag{4.6}$$

for N_p preamplifiers. To determine the total voltage, $\tilde{V}_o$, the output voltage of a single preamplifier, $\tilde{V}_{o1}$ is defined. By the principle of superposition, the output voltage of the

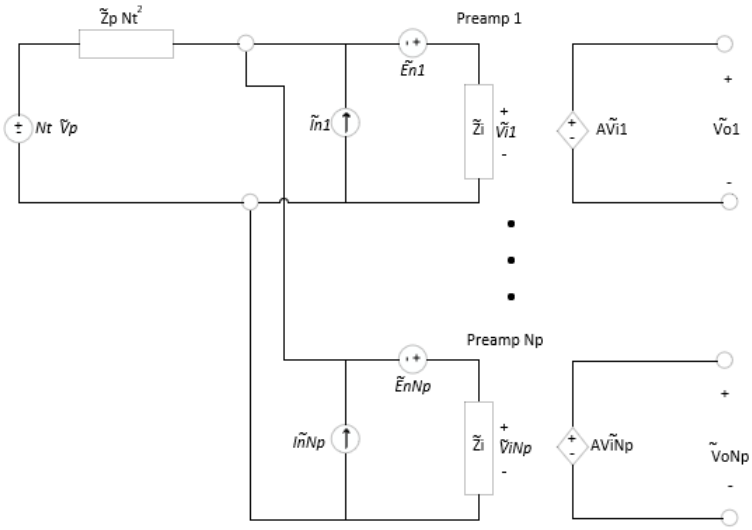

Figure 4.2. Probe and amplifier network where the transformer is assumed to be an ideal transmission line transformer.

first preamp, $\tilde{V}_{o1}$ is

$$\tilde{V}_{o1} = \tilde{V}_{o1}\Big|_{\tilde{V}_p} + \tilde{V}_{o1}\Big|_{\tilde{E}_{n1}} + \sum_{k=2}^{N_p} \tilde{V}_{o1}\Big|_{\tilde{E}_{nk}} + \tilde{V}_{o1}\Big|_{\tilde{I}_{n1}} + \sum_{k=2}^{N_p} \tilde{V}_{o1}\Big|_{\tilde{I}_{nk}} . \tag{4.7}$$

The first term in Eq. (4.7) represents the output voltage due to the thermal noise voltage of the probe. To determine $\tilde{V}_{o1}$, all sources except $\tilde{V}_p$ are deactivated in which all voltage sources are shorted and all current sources are opened. The result of deactivating all sources except $\tilde{V}_p$ is

$$\tilde{V}_{o1}\Big|_{\tilde{V}_p} = A\frac{\tilde{Z}_i/N_p}{(\tilde{Z}_i/N_p) + \tilde{Z}_p N_t^2} N_t \tilde{V}_p. \tag{4.8}$$

Next, the output voltage due to a single voltage source, $\tilde{E}_{n1}$ is determined by deactivating all sources except $\tilde{E}_{n1}$ to obtain

$$\tilde{V}_{o1}\Big|_{\tilde{E}_{n1}} = A\frac{\tilde{Z}_i}{\tilde{Z}_i + (\tilde{Z}_i/N_{p-1})||(\tilde{Z}_p N_t^2)} \tilde{E}_{n1}. \tag{4.9}$$

Similarly, the output voltage due to a single current source, $\tilde{I}_{n1}$ is determined by deactivating all sources except $\tilde{I}_{n1}$ to obtain

$$\tilde{V}_{o1}\Big|_{\tilde{I}_{n1}} = A\left(\frac{\tilde{Z}_i}{N_p}\right)||(\tilde{Z}_p N_t^2)\tilde{I}_{n1}. \tag{4.10}$$

Lastly, the output voltage of the first op amp due to the voltage sources of the parallel op amps is the sum of N_p - 1 output voltages, $\tilde{V}_{o1}$ for which all sources are deactivated except the specified voltage source, $\tilde{E}_{nk}$. The sum of the output voltages due to the parallel voltage sources is

$$\sum_{k=2}^{N_p} \tilde{V}_{o1}\Big|_{\tilde{E}_{nk}} = A\frac{\left(\frac{\tilde{Z}_i}{N_{p-1}}\right)||(\tilde{Z}_p N_t^2)}{\tilde{Z}_i + \left(\frac{\tilde{Z}_i}{N_{p-1}}\right)||(\tilde{Z}_p N_t^2)}\tilde{E}_{nk} \text{ for k = 2, ..., } N_p. \tag{4.11}$$

Similarly, the output voltage of the first op amp due to the current sources of the parallel op amps is the sum of N_p - 1 output voltages, $\tilde{V}_{o1}$ for which all sources are deactivated except the specified current source, $\tilde{I}_{nk}$. The sum of the output voltages due to the parallel current sources is

$$\sum_{k=2}^{N_p} \tilde{V}_{o1}\Big|_{\tilde{I}_{nk}} = A(\tilde{Z}_p N_t^2)||(\tilde{Z}_i)\tilde{I}_{nk} \text{ for k = 2, ..., } N_p. \tag{4.12}$$

Now that all the terms for a single output voltage, $\tilde{V}_{o1}$ are defined, Eq. (4.6) is

$$\tilde{V}_o = \sum_{j=1}^{N_p}\left(\tilde{V}_{oj}\Big|_{\tilde{V}_p} + \tilde{V}_{oj}\Big|_{\tilde{E}_{nj}} + \sum_{k=2}^{N_p}\tilde{V}_{oj}\Big|_{\tilde{E}_{nk}} + \tilde{V}_{oj}\Big|_{\tilde{I}_{nj}} + \sum_{k=2}^{N_p}\tilde{V}_{oj}\Big|_{\tilde{I}_{nk}}\right). \tag{4.13}$$

The output voltage due to the thermal noise voltage of the probe is

$$\sum_{j=1}^{N_p}\tilde{V}_{oj}\Big|_{\tilde{V}_p} = A\frac{\tilde{Z}_i/N_p}{(\tilde{Z}_i/N_p) + \tilde{Z}_p N_t^2}N_t N_p \tilde{V}_p \tag{4.14}$$

because it does not depend on which preamplifer out of N_p is chosen. The output voltages due to a single voltage, E_{nj} or current source, I_{nj}, will linearly add to become

$$\sum_{j=1}^{N_p}\tilde{V}_{oj}\Big|_{\tilde{E}_{nj}} = A\frac{\tilde{Z}_i}{\tilde{Z}_i + (\tilde{Z}_i/N_{p-1})||(\tilde{Z}_p N_t^2)}\sum_{j=1}^{N_p}\tilde{E}_{nj}, \tag{4.15}$$

and

$$\sum_{j=1}^{N_p}\tilde{V}_{oj}\Big|_{\tilde{I}_{nj}} = A\left(\frac{\tilde{Z}_i}{N_p}\right)||(\tilde{Z}_p N_t^2)\sum_{j=1}^{N_p}\tilde{I}_{nj} \tag{4.16}$$

respectively. Lastly, the terms that depend on multiple voltage sources, E_{nk} or current sources, I_{nk} will have a factor of N_{p-1} as a result of the summation included in the

calculation of the output voltage for each op amp. The output voltages due to the multiple voltage sources and current sources are

$$\sum_{j=1}^{N_p}\sum_{k=2}^{N_p}\tilde{V}_{oj}\Big|_{\tilde{E}_{nk}} = A\frac{\left(\frac{\tilde{Z}_i}{N_{p-1}}\right)||(\tilde{Z}_pN_t^2)}{\tilde{Z}_i+\left(\frac{\tilde{Z}_i}{N_{p-1}}\right)||(\tilde{Z}_pN_t^2)}(N_{p-1})\sum_{j=1}^{N_p}\tilde{E}_{nj}, \tag{4.17}$$

and

$$\sum_{j=1}^{N_p}\sum_{k=2}^{N_p}\tilde{V}_{oj}\Big|_{\tilde{I}_{nk}} = A(\tilde{Z}_pN_t^2)||(\tilde{Z}_i)(N_{p-1})\sum_{j=1}^{N_p}\tilde{I}_{nj} \tag{4.18}$$

respectively. Combining all five terms obtains the total output voltage

$$\begin{aligned}\tilde{V}_o = {} & A\frac{\tilde{Z}_i/N_p}{(\tilde{Z}_i/N_p)+\tilde{Z}_pN_t^2}N_tN_p\tilde{V}_p + A\frac{\tilde{Z}_i}{\tilde{Z}_i+(\tilde{Z}_i/N_{p-1})||(\tilde{Z}_pN_t^2)}\sum_{j=1}^{N_p}\tilde{E}_{nj} \\ & + A\left(\frac{\tilde{Z}_i}{N_p}\right)||(\tilde{Z}_pN_t^2)\sum_{j=1}^{N_p}\tilde{I}_{nj} + A\frac{\left(\frac{\tilde{Z}_i}{N_{p-1}}\right)||(\tilde{Z}_pN_t^2)}{\tilde{Z}_i+\left(\frac{\tilde{Z}_i}{N_{p-1}}\right)||(\tilde{Z}_pN_t^2)}(N_{p-1})\sum_{j=1}^{N_p}\tilde{E}_{nj} \\ & + A(\tilde{Z}_pN_t^2)||(\tilde{Z}_i)(N_{p-1})\sum_{j=1}^{N_p}\tilde{I}_{nj}. \end{aligned} \tag{4.19}$$

Assume, $Z_i >> Z_p$, then Eq. (4.19) becomes

$$\tilde{V}_o = AN_tN_p\tilde{V}_p + A\sum_{j=1}^{N_p}\tilde{E}_{nj} + AN_p\tilde{Z}_pN_t^2\sum_{j=1}^{N_p}\tilde{I}_{nj}. \tag{4.20}$$

Similarly to Chapter 3, to find the squared RMS output voltage, $v_{o,rms}^2$, the noise sources are assumed to be statistically independent and therefore, their cross terms vanish [26]. Using this assumption, the squared RMS output voltage is

$$v_{o,rms}^2 = A^2N_t^2N_p^2v_{p,rms}^2 + A^2N_pe_n^2 + A^2N_p^2|\tilde{Z}_p|^2N_t^4i_n^2. \tag{4.21}$$

Finally, Eq. (4.5) can be written in which the numerator is Eq. (4.21) and the output voltage due to the thermal noise voltage of the probe is

$$v_{o,rms}^2|_{\text{due to } v_p \text{ of the coil}} = N_t^2N_p^2v_{p,rms}^2. \tag{4.22}$$

After simplification, the noise factor for a 1 kHz bandwidth is

$$F = 1 + \frac{\frac{e_n^2}{N_t^2 N_p} + i_n^2 |Z_p^2| N_t^2 N_p}{4KTR_p} \tag{4.23}$$

as given in Section 4.1.1.This equation for noise factor has been confirmed as derived in other sources [17, 26, 27]. Section 4.2 uses the noise factor equation shown in this section to discuss how the design parameters are chosen to minimize the noise factor.

4.2 Design Selection

This section applies the parallel LNA design used by Zheng in an MPI system to a QR detection system [26]. The first subsection shows the topology of the design which includes the selection of turns ratio, N_t and the number of parallel LNAs, N_p. The second subsection explains the selection of the LNAs, the summing amplifier, and the resistor and capacitor values. The final subsection shows simulation results consisting of the transient response and the noise simulation.

4.2.1 Topology

The goal of the design is to minimize the noise factor given in Eq. (4.23) by focusing on two key terms: the e_n term and the i_n term. The i_n term contains the magnitude of the probe impedance $|Z_p|$, which is frequency dependent. Therefore, the design aims to first, make this term approach 0 and second, minimize the e_n term. Designing the topology and selecting the components for this network considers the impact on the e_n term or the i_n term.

Figure 4.3 shows the design layout consisting of the probe and step-up transformer, the first stage with LNAs, and the second stage with a summing amplifier. For the convenience of viewing the components, this figure only shows one of the N_p LNAs. Appendix A shows the complete layout with all 8 LNAs in parallel.

The transformer is designed to behave as a transmission-line transformer that steps up the load impedance independent of the signal frequency [29]. The turns ratio is given as 1:N_t where N_t is chosen to increase the input impedance without coupling into the transformer. As the turns ratio increases, the transformer behaves less like a transmission line transformer and becomes frequency dependent. As a result, it no longer behaves as an ideal transformer with the desired turns ratio. For the Raytheon system, the optimal

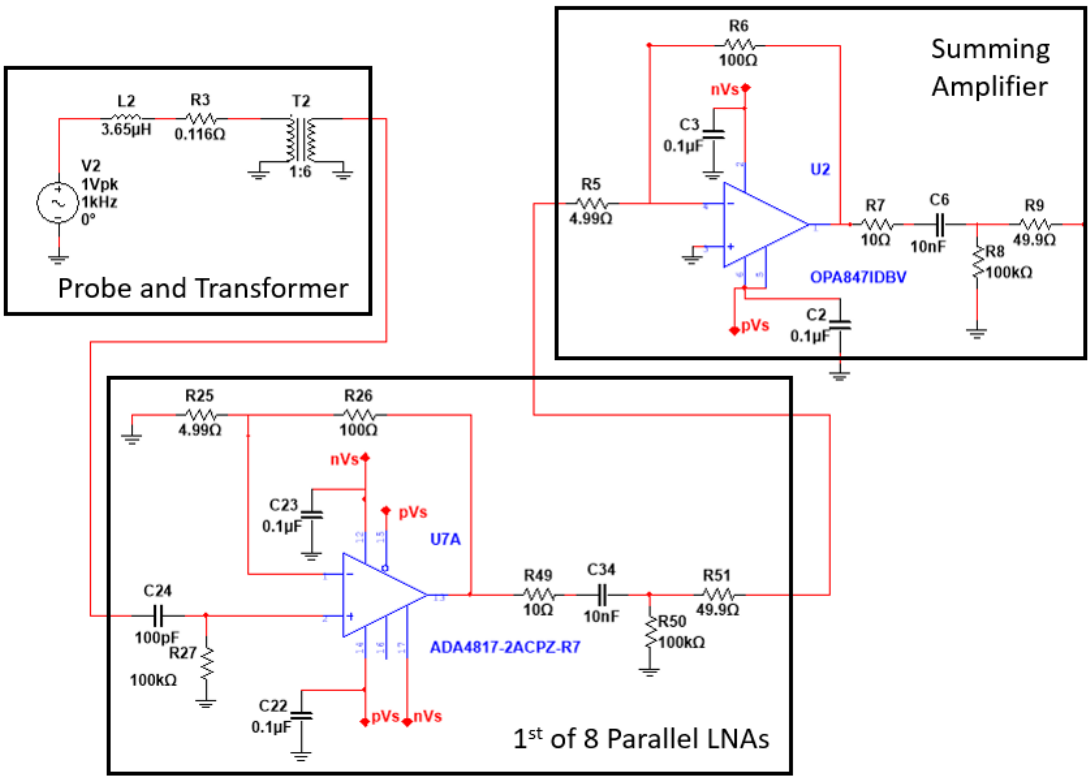

Figure 4.3. Multisim configuration of broadband design with a receiver probe, a step-up transformer, 1 of the 8 parallel LNAs with input and output circuits, and the summing amplifier with input and output circuit.

turns ratio before the ideal transformer assumption begins to breakdown is 1:6.

The number of parallel devices, N_p is chosen to minimize the impact of the voltage noise source, e_n [26]. In Zheng's MPI application, the optimal value of N_p is 24 which provides some insight of a range for N_p [26]. For the work in this thesis, Multisim simulations confirmed a N_p value of 8 achieved the optimal noise factor across the entire band of frequencies. The next section discusses the selection of the op amps and values of the capacitors and resistors in terms of gain setting, an input network, and an output network.

4.2.2 Component Selection

To begin, the impedance of the probe and the thermal voltage due to the resistance of the probe are not manipulated when determining these design parameters. The factors e_n and i_n can be made small by choosing an op amp with low current and voltage noise sources. The op amp for the first stage design is an ADA4817-2 with voltage noise, e_n

of 4 nV/$\sqrt{Hz}$, current noise, i_n of 2.5 fA/$\sqrt{Hz}$, input capacitance of 1.3 pF and -3 dB bandwidth of 1050 MHz making it an ideal low-noise broadband op amp [28].

The second stage is an OPA847 configured as an inverting summing amplifier that will average the first stage of op amps. The OPA847 has e_n of 0.85 nV/$\sqrt{Hz}$ and i_n at 2.5 pA/$\sqrt{Hz}$ [30]. All of the op amps used in this design have bypass capacitors of 0.1 μF that limit the amplifier's noise from coupling into the power pins [28, 30].

The gain-setting resistors on both the first stage and the second stage were chosen to be low-valued to limit the thermal noise contribution. All of the resistors used in the Multisim models are values with a 1% tolerance to make the simulations as realistic to a prototype as possible. The first stage was designed to have a low gain of 21 to tolerate any slight variance in the output voltage of the parallel devices [26]. The gain of the second stage, which was designed to be 8, creates a total gain, beginning with the first stage of op-amps, of 168 (45 dB). Taking into account the step-up transformer with a turns ratio of 6, the total gain of the system beginning at the probe, is 1008 which is 60 dB and agrees with the simulation shown in Section 4.2.3.1.

At the output stage of every op amp is a series 10 Ω resistor referred to as R_{snub}. Driving capacitive loads will produce a peak in the frequency response but R_{snub} creates a zero to cancel this pole and effectively, minimize the peak [25]. To apply this across the bandwidth, the value of R_{snub} should range between 10 Ω to 50 Ω [28]. Following R_{snub} is a serial capacitor and a parallel resistor that set the high-frequency roll-off [25]. The values were chosen to move the resonant peak in the frequency response beyond the desired bandwidth. Lastly, the serial resistor of 50 Ω balances the load current among the devices [26].

The input circuit to the first stage contains a 100 pF capacitor and a 100 kΩ resistor to form a high pass filter. The low-valued components were chosen to limit thermal noise contribution while controlling the low-frequency cutoff necessary for a broadband application [25]. In particular, through simulation, it was found that increasing the serial capacitor above 100 pF would result in a low-frequency cut-off greater than 400 kHz. The next section will demonstrate the simulations of the noise factor and transient response of the design discussed in this section.

4.2.3 Simulations

This section provides a demonstration of the predicted performance of the broadband, parallel LNA design. The first subsection shows the noise factor results as simulated in Multisim. The second subsection shows the transient response in which the dead time

has significantly reduced in comparison to the matching network of Chapter 3.

4.2.3.1 Noise Factor

Appendix A shows the Multisim configuration of the input signal from the voltage source, the probe modeled by its equivalent impedance, the step-up transformer with a turns ratio of 6, and the 8 parallel, non-inverting ADA4817 LNA's that are summed in the inverting OPA847IDBV with an output to the bode plotter.

The data from the bode plotter in the Multisim configuration is plotted in Figure 4.4 with Matlab code shown in Appendix B. This figure plots the magnitude and phase of the frequency response. As shown in the magnitude plot of Figure 4.4, the center frequency has a maximum gain of 60 dB with a 3 dB bandwidth from 164 kHz to 6.4MHz. Additionally, this plot shows a resonant peak at 4.2 MHz. The desired bandwidth for this thesis project ranges from AN at 423 kHz to C-4 at 3.410 MHz therefore, the desired bandwidth is contained in the 3 dB bandwidth and the resonant peak is outside the range of detection. The phase plot shows a crossover frequency at 3.4 MHz which confirms that the peak in the magnitude plot is a resonant peak formed by the circuit.

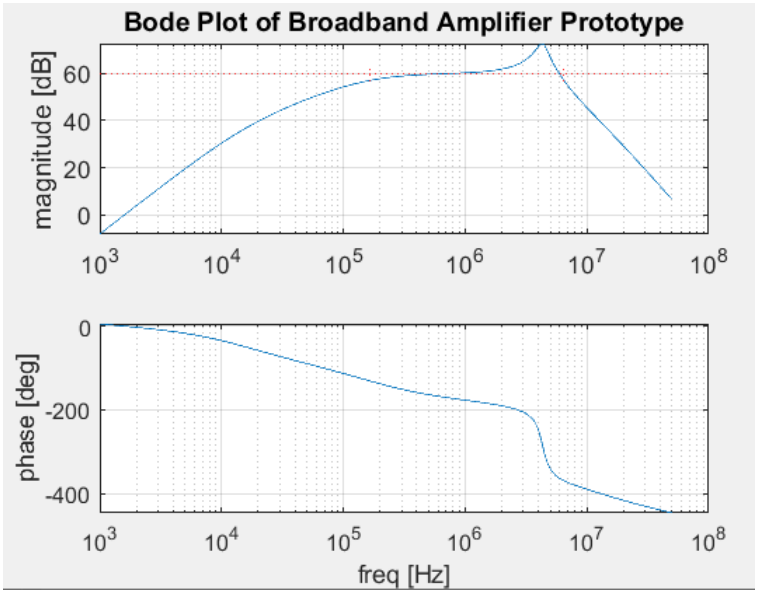

Figure 4.4. Frequency response of the broadband amplifier prototype with 3 dB bandwidth from 164 kHz to 6.4 MHz and a resonant peak at 4.2 MHz.

Appendix C shows the noise simulation in Multisim of the broadband design which plots the power spectral density (PSD) curves against frequency. The PSD curves for "rr3" and "spectrum" correspond to the resistors, R3, right before the transformer, and

R9, after the output circuit of the summing amplifier, respectively. The cursors are placed around the bounds of the desired bandwidth, 423 kHz to 3.401 MHz. The noise figure is calculated by

$$NF = 10\log_{10}\left(\frac{(\text{rr3}_{rms})^2}{(\text{spectrum}_{rms})^2}\right). \tag{4.24}$$

The results of the noise figure calculation are shown in Table 4.1 for the minimum and maximum noise figure of the LNA amplifier design.

Freq [Hz]	SNR_i $[\frac{V_{rms}}{\sqrt{Hz}}]$	SNR_o $[\frac{V_{rms}}{\sqrt{Hz}}]$	NF [dB]
423.27 k	41.04 n	233.49 n	15.10
3.4077 M	102.91 n	1.375 u	22.52

Table 4.1. Minimum and maximum noise figure within the bandwidth of the receiver network for the broadband design.

Comparing these noise figure results to the series-parallel matching network of Chapter 3 that achieves a noise factor of 0.3 dB, the broadband design does not seem ideal. In the next section, the transient response shows that the dead time of the broadband design is significantly less than the matching network as a tradeoff for the increase in noise factor.

4.2.3.2 Transient Response

The transient response as shown in Figure 4.5 shows how the amplifier network responds to the switching of the RF excitation pulse which is important because it determines the dead time required to quickly dissipate the stored energy as discussed in Chapter 2. Appendix E shows the Multisim configuration for the broadband design with a burst input signal. The blue curve is a 423 kHz sine wave with an amplitude of 100 mV. The red curve represents the de-Q switch which is pulsed at a frequency of 100 kHz to simulate a pulse sequence. The green curve is the transient response. Figure 4.5 shows the transient response when the RF pulse turns off and a ringdown with a time constant of approximately 0.8 μs is observed. With five time constants, or 4 μs, the signal level is below a level of concern.

As mentioned in Chapter 3, the matching network approach typically requires a dead time of 1 ms. Section 4.3 explains how the decrease in dead time improves the measurement SNR of the parallel LNA design.

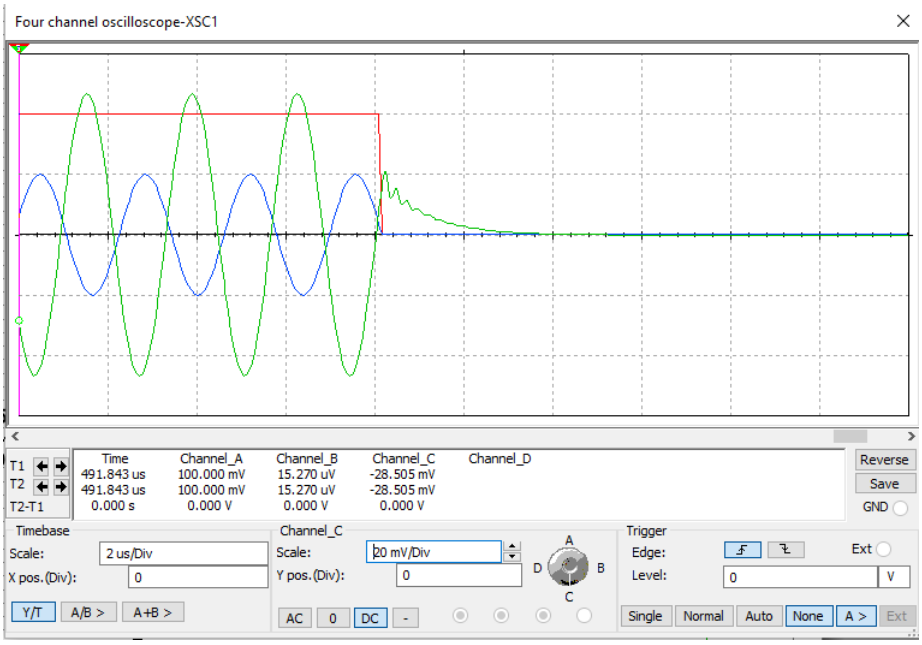

Figure 4.5. Transient response to a burst sine wave with a dead time of 4 μs. The red curve is the switch controlling the pulse sequence. The blue curve is the output signal controlled by the switch. The green curve is the transient response at the output of the amplifier network.

4.3 Performance in a QR Detection System

This section proves that the broadband prototype design has a predicted performance that is comparable with that of the matching network of Section 3.2.

In comparison to a 1 ms dead time required for a system with a resonant matching network, 4 μs is a significant change. By eliminating this dead time, the time-to-echo, T_E can be reduced which correlates to faster pulsing. As will be shown in the following simulation, faster pulsing due to a smaller T_E is directly related to improving the SNR. In Eq. (2.3) the effective spin-spin relaxation time constant, $T_{2,eff}$ is inversely proportional to the time-to-echo.

Figure 4.6 shows the pulse sequence used for a system with a resonant matching network as shown in Section 3.2 in which the dead time required to dissipate the stored energy and avoid ringdown is 1 ms. The standard pulse width and time-to-echo are 1 ms and 3 ms, respectively. Therefore, the length of the data acquisition window will be 1 ms. For a standard SLSE sequence, the time delay between successive sequences, T_d is 1 ms with consideration of the time constant, T_1 required for the nuclei to return to thermal equilibrium.

Figure 4.7 shows the pulse sequence used for a broadband, non-resonant system as

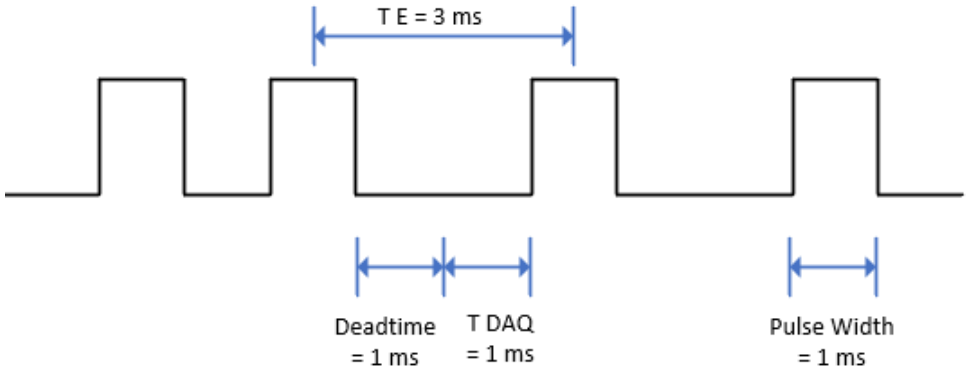

Figure 4.6. Pulse sequence for matching network design: 1 ms of dead time, 1 ms for acquiring data, 3 ms for the time to echo, and 1 ms pulse width.

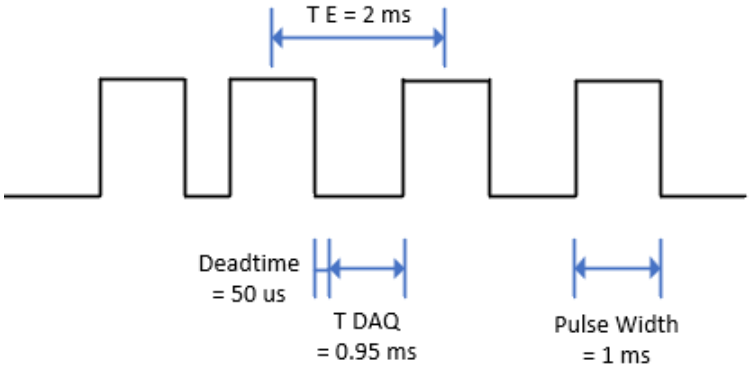

Figure 4.7. Pulse sequence for parallel LNA design: reduced dead time creates a smaller time to echo while pulse width and the length of the data acquisition window remain the same.

shown in Section 4.2 in which the dead time required to dissipate the stored energy and avoid ringdown is a conservative value of 50 μs. The pulse width remains as 1 ms while the time-to-echo can be shortened to 2 ms. The length of the data acquisition window, T_{DAQ} is now 0.94 ms, which is roughly the same as the T_{DAQ} for the matching network. The time delay between successive sequences, T_d cannot be shortened because the time constant T_1 is not changed.

Appendix D shows the code used to generate a pair of SLSE sequences with 500 echoes per sequence for the two cases shown in Figure 4.6 and 4.7. Figure 4.8 shows the magnitude in dB of the average spin-echo frequency response between cases 1 and 2. Using the data points in this figure, the signal in case 2 gained 19.44 dB by pulsing faster. However, since the broadband system is not noise-less, the noise floor has also increased.

The standard noise figure, NF for a system with a matching network is 0.3 dB while

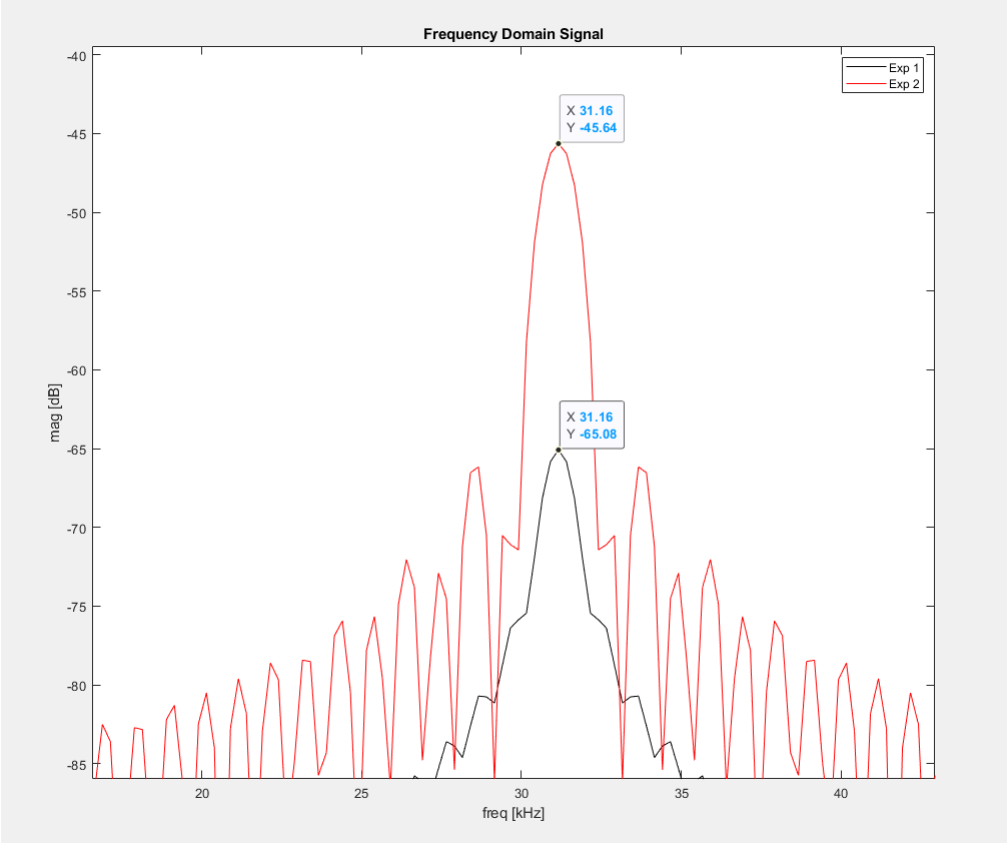

Figure 4.8. MATLAB plot of change in gain in dB of the frequency domain signal of the average spin echo for experiment 1 with 1 ms of dead time and experiment 2 with 50 μs of dead time.

Section 4.2 shows the noise figure of the broadband amplifier is 15 dB at best and 22 dB at worst. In the worst case, the noise figure of the broadband amplifier increased by 21.7 dB by pulsing faster in comparison to a design that cannot afford to reduce dead time.

Since the signal gained 19.44 dB and the noise increased by 21.7 dB, the broadband design only lost 2.26 dB in SNR by using a smaller time-to-echo. Comparing the 2.26 dB loss in SNR to the increase in detection time due to the time to tune for the matching network, the SNR loss is a smaller cost to detection time.

Chapter 5
Discussion and Future Work

The work in this thesis presents a broadband preamplifier prototype in comparison to the conventional series-parallel matching network design. However, in Chapter 4, the broadband design using a single silicone JFET was discussed but ultimately, ruled out because the unique component is no longer manufactured. This chapter will explore the possibility of a better design if the optimal JFET was accessible. The first section will summarize the key results of this thesis and the second section will discuss the silicone JFET design.

5.1 Key Results

Chapter 3 provided insight into the conventional receiver design for NQR detection systems. Although the design has produced an optimal noise factor by noise matching to an amplifier, the time to tune the C_p and C_s components and the ringing due to the resonant circuit that is formed, makes this system unrealistic for commercialization.

Chapter 4 has shown an alternative approach that focuses on amplifying the QR signal with low-noise amplifiers while reducing the noise of the system with signal averaging. In addition, since this design does not form a resonant circuit within the detection frequency band and does not require tuning, the system has a significantly smaller detection time compared to the matching network.

The broadband design has a noise figure of 15 dB in the low-frequency range and 22 dB in the higher-frequency range. The components are all easily accessible for a prototype design. In comparison to the matching network, the broadband design lost 2.26 dB in exchange for eliminating the time to tune to new frequencies.

The broadband design could be improved by reducing the noise figure. Section 5.2 will explore the possibility of optimizing the noise factor by exchanging components in

the broadband design.

5.2 Next Steps

In Section 4.1, the use of a transformer-like network and set of parallel LNAs has been successfully modeled for an MPI system with a frequency range of 10 kHz to 200 kHz [26]. Unlike an MPI system, the desired bandwidth of a QR detection system can range up to 3.5 MHz. In comparison, Mandal's non-tuning, MR system with a step-up transformer followed by a single JFET, successfully measured the QR spectrum of glycine which ranges from 0.3 MHz to 1.1 MHz [17].

The method for transmitting in Mandal's [17] system resembles the pulse sequence used in QR detection systems, and therefore the concerns and mitigation regarding a transient response from RF pulses in Chapter 2 would not change with the use of the JFET from Mandal's design. The main difference between the QR system architecture and Mandal's system architecture is the impedance of the inductive sensor. As shown in Table 5.1, the resistance of the probe in the JFET experiment is larger than the NQR probe by a factor of about 4 while the reactance is comparable [17].

The key design differences between the JFET design and the parallel LNA design are summarized in Table 5.1. The parameters chosen for this table can be directly applied to the noise factor equation in Section 4.1. The summing amplifier in the parallel LNA design is not included because it has a small noise factor contribution in comparison to the first stage of this design [31].

	e_n [nV/$\sqrt{Hz}$]	i_n [fA/$\sqrt{Hz}$]	C_{in} [pF]	L_p [μH]	R_p [Ω]	N_t	N_p
JFET	0.8	18	10	15	1.88	6	1
LNA	4	2.5	1.3	3.65	0.116	6	8

Table 5.1. Design parameters for MR system using JFET and NQR detection system using parallel LNAs.

Figure 5.1 shows the experimental results for Mandal's design in which the noise figure can become as low as 1 dB in the NQR frequency range [17]. Mandal shows a noise figure of 1.2 dB at 2 MHz. In comparison, the parallel LNA design from Chapter 4 yields a predicted noise figure of 18 dB at 2 MHz that can be calculated from Figure 5.2. The noise figure is not a fair comparison between the performance of the two systems because the noise figure only represents a ratio of input SNR and output SNR. Therefore, without considering the possibility of a difference in input SNR, a lower noise figure does

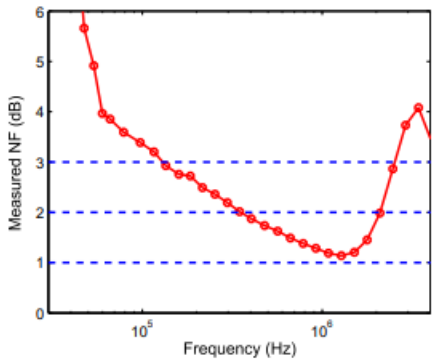

Figure 5.1. Measured noise figure at the output of the receiver in an MR system with probe resistance of 1.88 Ω [17]

Cursor	onoise_rr3	onoise_spectrum
x1		
y1		
x2	2.0042M	2.0042M
y2	54.4120n	447.5208n

Figure 5.2. Multisim noise simulation results at 2 MHz for the parallel LNA design where spectrum is the output noise voltage of the amplifier and rr3 is the input noise voltage.

not directly correspond to a better measurement SNR.

Using the noise figures mentioned above, the calculated noise factor of the JFET and parallel LNA designs are 1.32 and 63.08, respectively. Recall from Chapter 3 that the noise factor is the ratio of the input SNR over the output SNR where the input SNR is

$$SNR_i = \frac{v_{s,rms}^2}{4KTR_p}. \tag{5.1}$$

Using the relationship between noise factor and SNR, the output SNR can be defined as

$$SNR_o = \frac{v_{s,rms}^2}{4KTR_pF} \tag{5.2}$$

in terms of noise factor, the input QR signal voltage, Boltzmann's constant, the temperature in Kelvin and the resistance of the probe.

Since the input QR signal and temperature are consistent in both designs, the ratio

of the output SNR for the JFET design and the parallel LNA design simplifies to

$$\frac{SNR_{o,LNA}}{SNR_{o,JFET}} = \frac{R_{p,JFET}F_{JFET}}{R_{p,LNA}F_{LNA}}. \tag{5.3}$$

With the probe resistances from Table 5.1 and noise factors mentioned above, the ratio of output SNR is 0.34. This result shows that the output SNR of the parallel LNA design is 4.68 dB lower than the output SNR of the JFET design. This difference in output SNR is likely due to the higher e_n of the LNAs in comparison to the e_n of the JFET.

Based on this result, it may be worth exploring the JFET design if there is a component with comparable e_n and i_n values to that of the NXP Semiconductors BF862 silicone JFET.

Appendix A
Multisim Layout of Broadband Prototype Design

A.1 Bode Configuration in Multisim of Broadband Amplifier

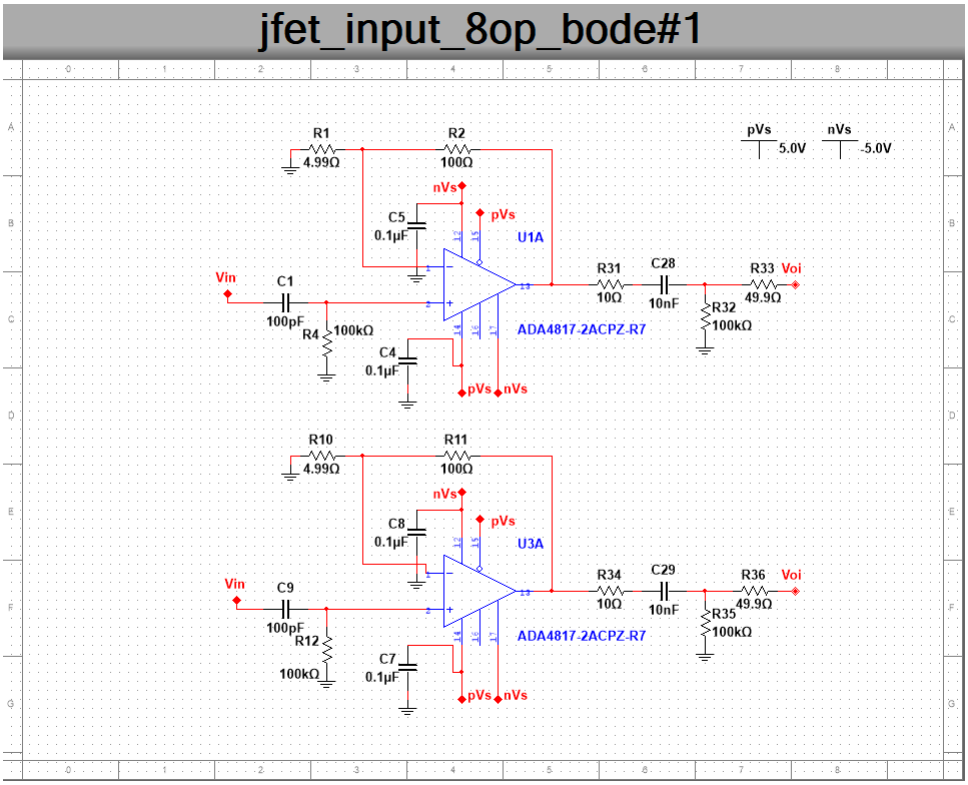

Figure A.1. Broadband amplifier design first stage parallel amplifiers 1 and 2.

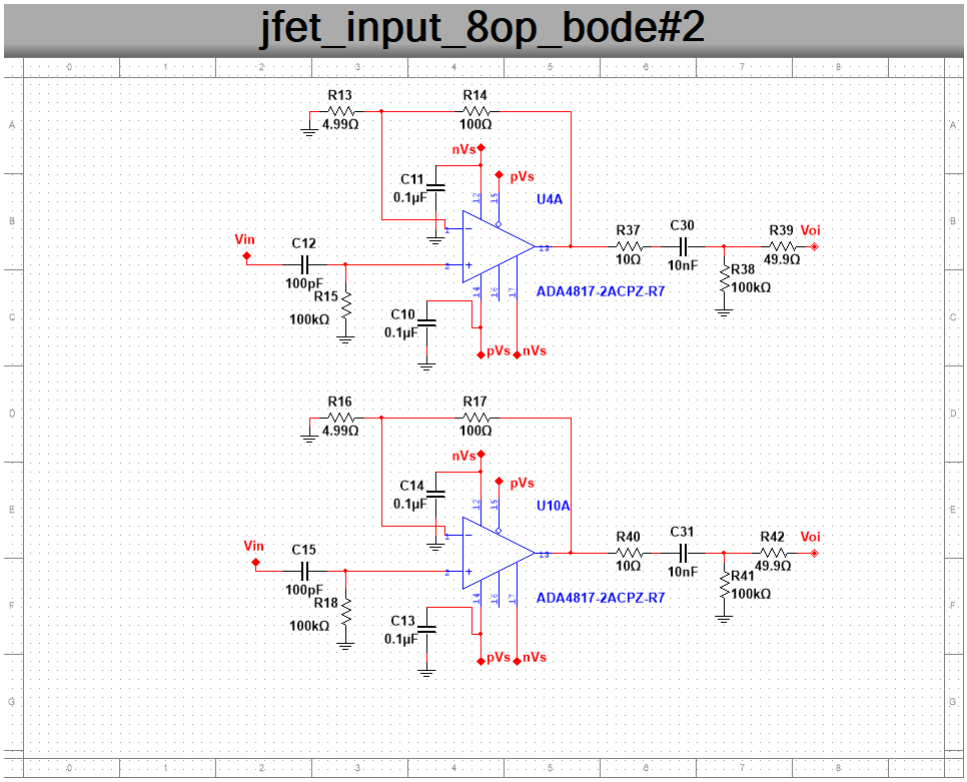

Figure A.2. Broadband amplifier design first stage parallel amplifiers 3 and 4.

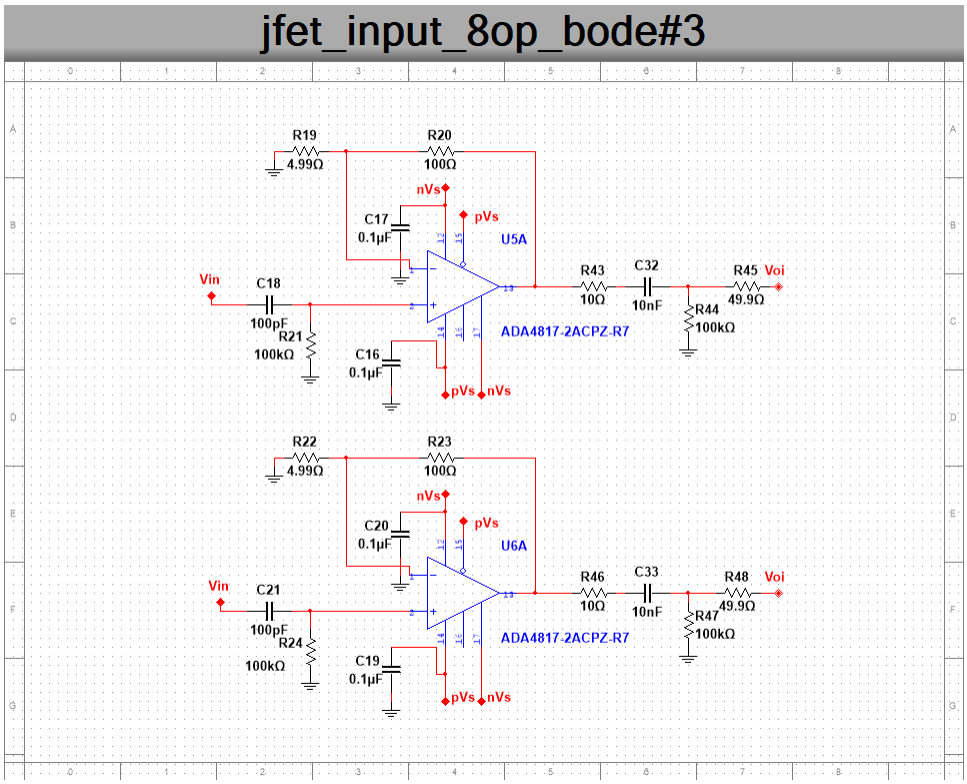

Figure A.3. Broadband amplifier design first stage parallel amplifiers 5 and 6.

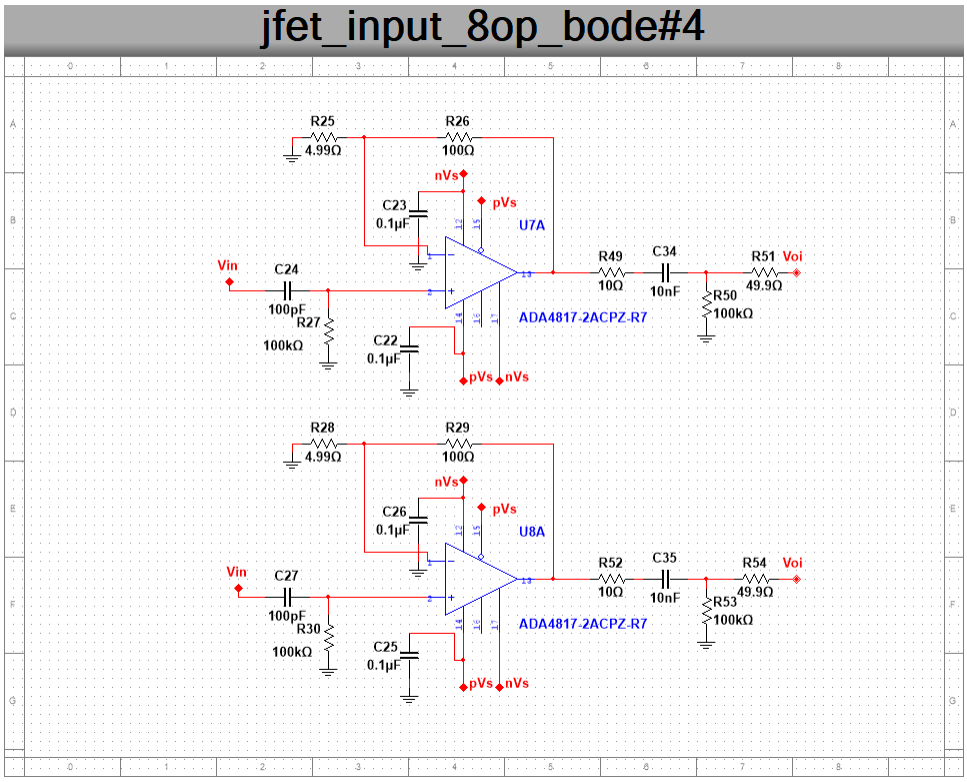

Figure A.4. Broadband amplifier design first stage parallel amplifiers 7 and 8.

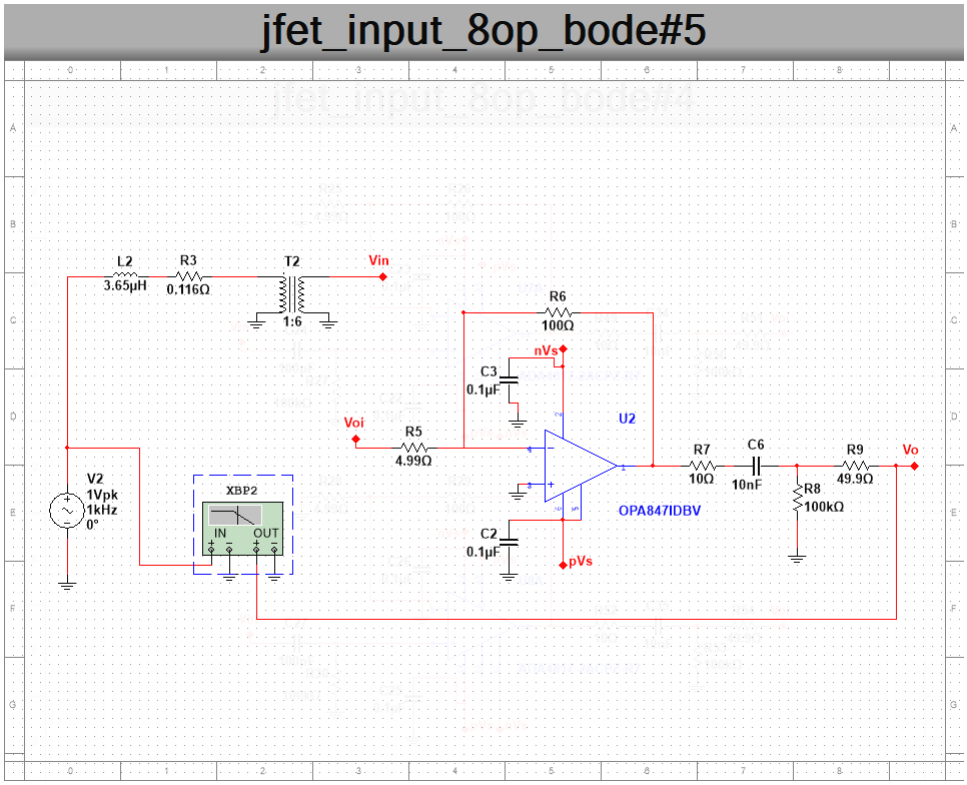

Figure A.5. Broadband amplifier design second stage summing amplifier.

Appendix B
Matlab Code

B.1 Matlab Code for Generating Bode Plot from Multisim Bode Data

```
%==========%
% m-file to bode data from
% Multisim simulation of broadband design
%==========%
% Multisim Simulation Parameters:
% Number of Points  = 1000
% Start Frequency = 1 kHz
% Final Frequency = 50 MHz
%==========%

load Multisim_Bode_Data.dat;

test = Multisim_Bode_Data;
f = test(:,1);
gain = test(:,3);
phase_deg = test(:,4);


gain_dB = 20*log10(gain);

idx = find( gain_dB > 60 - 3);
```

```
f_3dB_low = f(min(idx));
f_3dB_high = f(max(idx));

BW_3dB_MHz = (f_3dB_high - f_3dB_low)/1e6;



figure(1)
subplot(211)
semilogx(f, gain_dB, [min(f), max(f)], 60*[1,1], ':r',...
        [f_3dB_low, f_3dB_low], [60-3, 60+3], ':r',...
         [f_3dB_high, f_3dB_high], [60-3, 60+3], ':r')
grid on
FontSize = 14;
title('Bode Plot of Broadband Amplifier Prototype',...
    'FontSize', FontSize)
ylabel('magnitude [dB]', 'FontSize', FontSize);
ax = gca; ax.FontSize = 13;
subplot(212)
semilogx(f, phase_deg)
grid on
ylabel('phase [deg]', 'FontSize', FontSize);
xlabel('freq [Hz]', 'FontSize', FontSize);
ax = gca; ax.FontSize = 12;
```

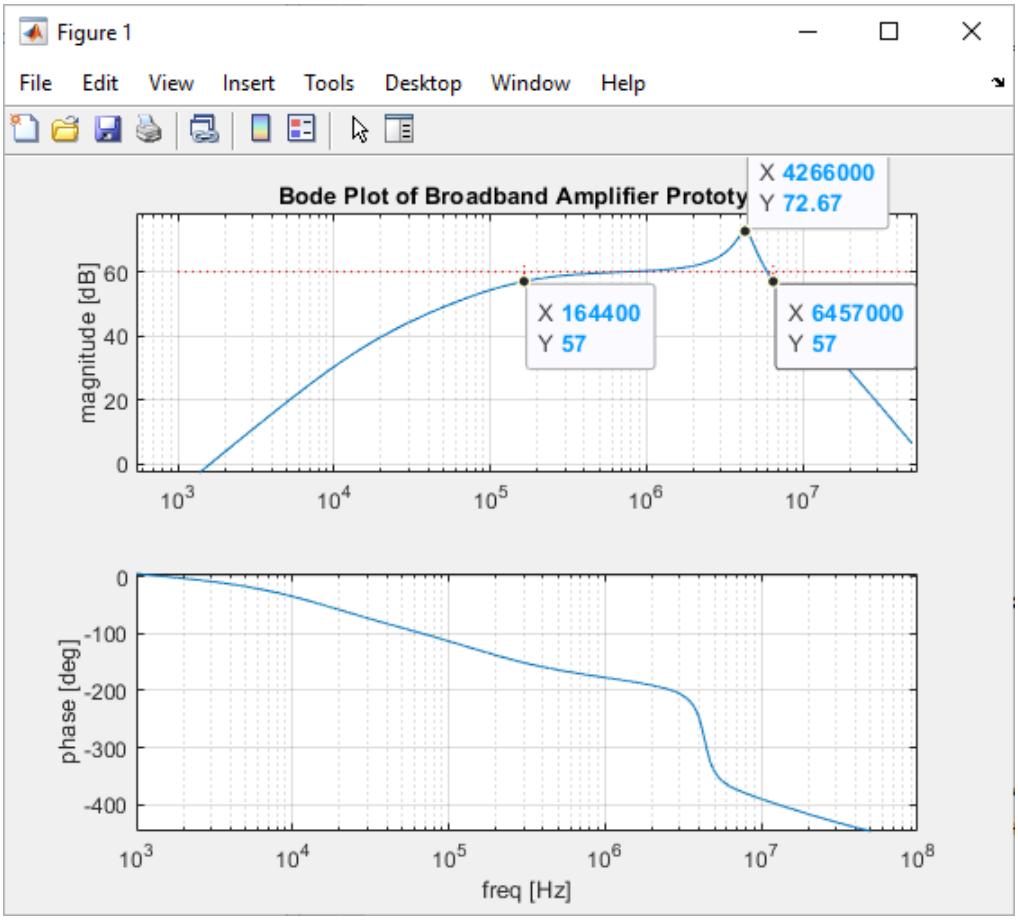

Figure B.1. Bode plot of broadband amplifier prototype with data points of 3 dB bandwidth from 164 kHz to 6.4 MHz and a resonant peak at 4.2 MHz.

Appendix C
Multisim Noise Analysis of Broadband Design

C.1 Multisim Noise Simulation

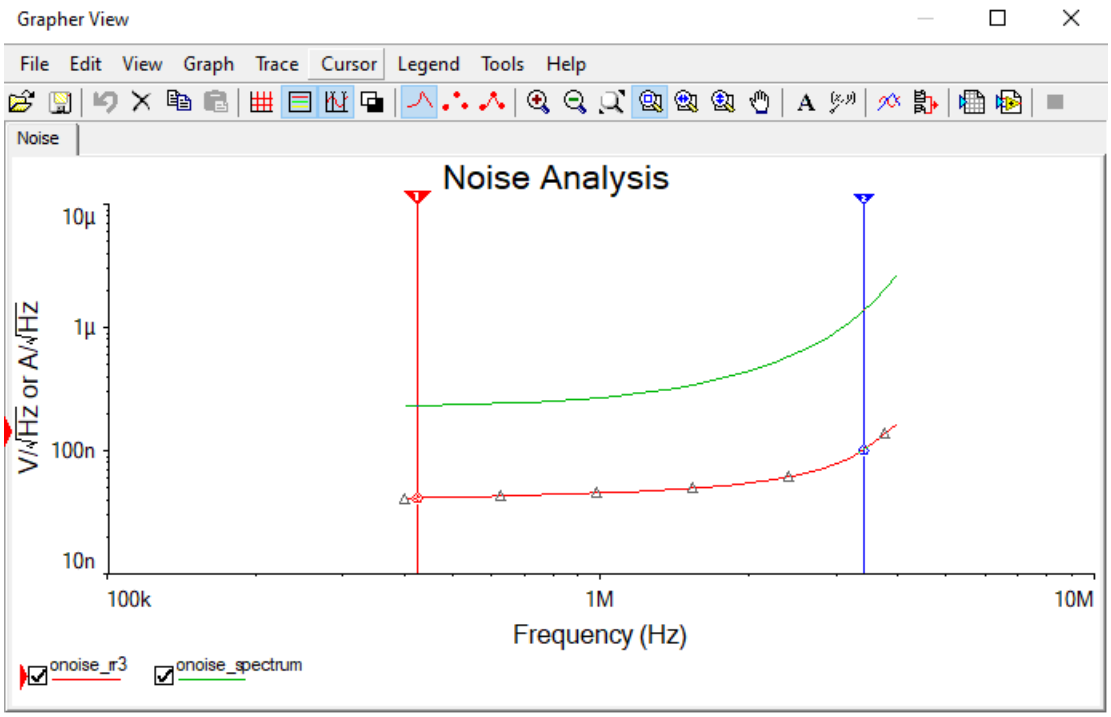

Figure C.1. Noise simulation at series resistor with the transformer and output of summing amplifier.

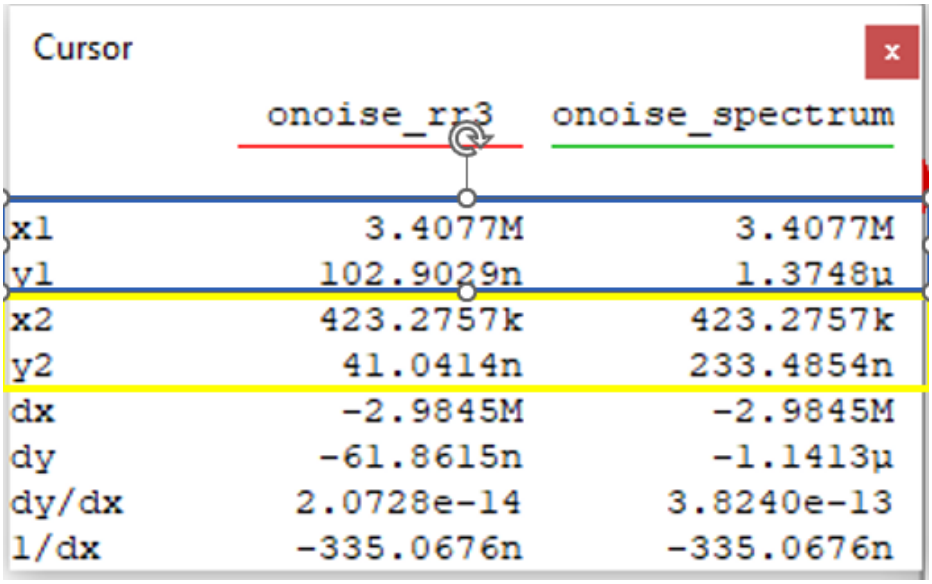

Figure C.2. Noise plot cursor values at 423 kHz and 3.4 MHz.

Appendix D
Matlab Code for Generating SLSE Pulse Sequence Reponse

D.1 Matlab Code of one SLSE Pulse Sequence

```
% Comapre average SLSE signals taking into
% account the dependency of the effctive T2 value
% on pulse spacing

% Clear the work space
clc; clearvars, close all

% dock the figures in one window
set(0,'DefaultFigureWindowStyle','Docked')


% N sequences = 2 (phase cycled; seq seperated T1)
% Ne = 500 per sequence

% T1 ~ 1sec

% SLSE sequence Exp 1
tau_1 = 3e-3;     % pulse spacing
tw_1  = 1.0e-3;  % pulse wdith
Td1   = 1.0e-3;  % deadtime
```

```
Ne_1  = 1000;     % number of echos
Tdaq_1 =  tau_1 - tw_1 - Td1;  % data acquisition window


% SLSE sequence Exp 2
tau_2 = 2.0e-3; % pulse spacing
tw_2  = 1.0e-3; % pulse wdith
Td2   = 50e-6;  % deadtime
Ne_2  = 1000;   % number of echoes
Tdaq_2 =  tau_2 - tw_2 - Td2;  % data acquisition window

% QR signal
fb    = 31e3;

T2s  = 0.5e-3;
T2e1 = 2e-3;
T2e2 = (tau_1/tau_2)^5 * T2e1;
A    = 1;

% baseband sample rate and period
fs = 250e3;
Ts = 1/fs;


% data acquistion window for Exp 1
t_start_1 = -tau_1/2 + tw_1/2 + Td1;
t_stop_1  =  t_start_1 + Tdaq_1;
t_acq_1   = (t_start_1: Ts : t_stop_1)';
Nt_1      = length(t_acq_1);

% data acquistion window for Exp 2
t_start_2 = -tau_2/2 + tw_2/2 + Td2;
t_stop_2  =  t_start_2 + Tdaq_2;
t_acq_2   = (t_start_2: Ts : t_stop_2)';
Nt_2      = length(t_acq_2);
```

```
% Generate average echo for Exp 1
echo_matrix_1 = zeros(Nt_1, Ne_1);
avg_echo_1    = zeros(Nt_1,1);
for echo_idx = 1   : Ne_1

   % generate echo
   echo_matrix_1(:,echo_idx) = A *...
        exp( -(echo_idx-1)*tau_1/T2e1)...
        * exp(-abs(t_acq_1)/T2s) .*...
        exp(1i*2*pi*fb*t_acq_1);

  % sum echos
  avg_echo_1 = avg_echo_1 + echo_matrix_1(:,echo_idx);

end
avg_echo_1 = avg_echo_1/Ne_1;


% Generate average echo for Exp 2
echo_matrix_2 = zeros(Nt_2, Ne_2);
avg_echo_2    = zeros(Nt_2,1);
for echo_idx = 1   : Ne_2

   % generate echo
   echo_matrix_2(:,echo_idx) = A *...
        exp( -(echo_idx-1)*tau_2/T2e2)...
        * exp(-abs(t_acq_2)/T2s) .*...
        exp(1i*2*pi*fb*t_acq_2);

  % sum echos
  avg_echo_2 = avg_echo_2+ echo_matrix_2(:,echo_idx);

end
```

```
avg_echo_2 = avg_echo_2/Ne_2;


% Determine freq domain representation
NPAD = 1000;
f = fs*linspace(-1/2, 1/2, NPAD);  %fvec 2-sided spectra
%
Smag_1 = abs( fftshift( fft(avg_echo_1, NPAD) )...
    / Nt_1);
Smag_dB_1 = 20*log10(Smag_1);
%
Smag_2 = abs( fftshift( fft(avg_echo_2, NPAD) )...
    / Nt_2);
Smag_dB_2 = 20*log10(Smag_2);

figure(1)
subplot(211)
plot(t_acq_1*1e6, real(avg_echo_1), '-k',...
    t_acq_1*1e6,...
    imag(avg_echo_1), '-r')
ylim([-0.1,0.1])
legend('in-phase', 'quadrature')
title('Average Echo Exp 1')
ylabel('Amplitude'); xlabel('time [us]')
subplot(212)
plot(t_acq_2*1e6, real(avg_echo_2), '-k',...
    t_acq_2*1e6,...
    imag(avg_echo_2), '-r')
ylim([-0.1,0.1])
title('Average Echo Exp 2')
ylabel('Amplitude'); xlabel('time [us]')

figure(2)
plot(f*1e-3, Smag_dB_1, '-k', f*1e-3, Smag_dB_2, '-r')
ylim([-150,0])
```

```
title('Frequency Domain Signal')
ylabel('mag [dB]'); xlabel('freq [kHz]')
legend('Exp 1', 'Exp 2')
```

Appendix E
Transient Response

E.1 Multisim Configuration for Transient Response

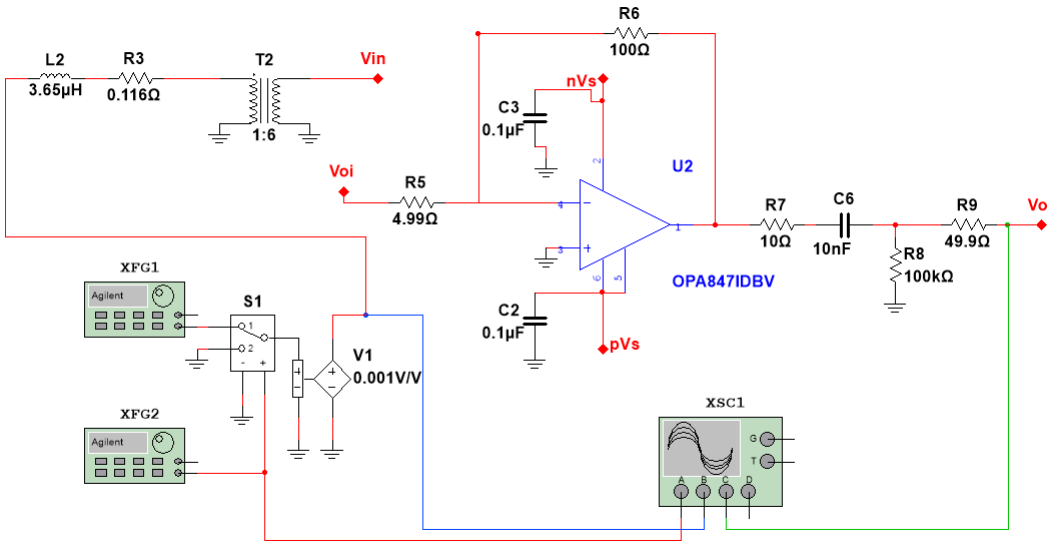

Figure E.1. Multisim configuration to simulate a pulsed sequence using a sine wave function generator, a square wave function generator, and a switch.

Bibliography

[1] A. N. Garroway, M. L. Buess, J. B. Miller, B. H. Suits, A. D. Hibbs, G. A. Barrall, R. Matthew and L. J. Burnett, "Remote sensing by nuclear quadrupole resonance," *IEEE Transactions on Geoscience and Remote Sensing*, vol. 39, no. 6, pp. 1108-1118, 2001.

[2] T. Hirschfeld and S. M. Klainer, "Short Range NQR Measurment," *Journal of Molecular Structure*, vol. 58, pp. 63-77, 1980.

[3] R. A. Marino, "Detection and identification of explosives by ^{14}N NQR," *Proceedings of New Concepts Symposium and Workshop on Detection and Identification of Explosives*, Virginia: Springfield, pp. 399–403, 1978.

[4] R. V. Pound, "Nuclear Electric Quadrupole Interactions in Crystals," Physical Review, vol. 79, no. 4, pp. 685-702, 1950.

[5] J. A. S. Smith, "Nuclear Quadrupole Resonance Spectroscopy," *Journal of Scientific Instruments*, vol. 48, no. 1, pp. 39-49, 1971.

[6] M. L. Buess, A. N. Garroway and J. B. Miller, "NQR detection using a meanderline surface coil," *Journal of Magnetic Resonance*, vol. 92, pp. 348-362, 1991.

[7] M. L. Buess, et al., "Detection of Explosives by Nuclear Quadrupole Resonance," US Patent 5 206 592, April 27, 1993.

[8] M. L. Buess, et al., "Detection of Explosives and Narcotics by Low Power Large Sample Volume Nuclear Quadrupole Resonance (NQR)," US Patent 5 233 300, Aug 3, 1993.

[9] M. L. Buess, et al., "Removing the Effects of Acoustic Ringing and Reducing Temperature Effects in the Detection of Explosives by NQR," US Patent 5 365 171, Nov. 15, 1994.

[10] "InVision Technologies Subsidiary Receives FAA Acceptance of Its Hold Baggage Scanning Systems; Also Completes FAA Field Trials of Cabin Baggage Screening System." *Business Wire*, Sept. 10, 1998.

[11] L. Thiesan, D. Hannam, D. W. Murray and J. E. Parmeter, "Survey of Commercially Available Explosives Detection Technologies and Equipment 2004," U.S. Department of Justice, Nov., 2004

[12] T. G. Lavedas, "Near-field Gradient Probe for the Suppression of Radio Interference," US Patent 0372395 A1, Dec. 4, 2015.

[13] R. A. Marino, "NQR/NMR Studies of Solid Phase Energetic Materials," *Chemistry and Physics of Energetic Materials*, pp. 715-738, 1990.

[14] R. R. Ernst, "Sensitivity enhancement in magnetic resonance: an analysis of the method of time averaging," *The Review of Scientific Instruments*, vol. 36, 1965.

[15] R. A. Marino and S. M. Klainer, "Multiple Spin Echoes in Pure Quadrupole Resonance," *The Journal of Chemical Physics*, vol. 67, no. 7, pp. 3388–3389, 1977.

[16] S. Letzer and N. Webster, "Noise in Amplifiers," *IEEE Spectrum*, August 1970.

[17] S. Mandal, S. Utzuzawa, D.G. Cory, M. Hürlimann, M. Poitzsch, and Y.-Q. Song, "An ultra-broadband low-frequency magnetic resonance system," *Journal of Magnetic Resonance*, vol. 242, pp. 113-125, 2014.

[18] T. P. Das and E. L. Hahn, *Nuclear Quadrupole Resonance Spectroscopy*, New York: Academic Press Inc., 1958.

[19] H. Nyquist, "Thermal Agitation of Electric Charge in Conductors," Physical Review, vol. 32, pp. 110–113, 1928.

[20] C. D. Motchenbacher and J. A. Connelly , *Low Noise Electronic System Design*, New York: Wiley, 1993.

[21] R. J. Karpowicz and T. B. Brill, "Librational Motion of Hexahydro-1,3,5-trinitro-s-triazine Based on the Temperature Dependence of the Nitrogen-14 Nuclear Quadrupole Resonance Spectra: The Relationship to Condensed-Phase Thermal Decomposition," *Journal of Physical Chemistry*, vol. 87, no. 12 pp. 2109-2112, 1983.

[22] K. E. Nixon and K. L. Sauer, "Pulsed spin-locking of spin-3/2 nuclei: ^{39}K-NQR of potassium chlorate," *Journal of Magnetic resonance*, vol. 335, 2022.

[23] W. Li, et al., "Broadband Matching of Nuclear Quadrupole Resonance Detector Using Non-Foster Circuits" Loughborough Antennas & Propagation Conference, 2016.

[24] H. Davoodi, et al., "Broadband and multi-resonant sensors for NMR" *Progress in Nuclear Magnetic Resonance Spectroscopy*, vol. 112-113, pp. 34-54, 2019.

[25] W. Jung, et al., *Op Amp Applications Handbook*, Analog Devices, 2002.

[26] B. Zheng, P. Goodwill, D. Xiao, W. Zheng, B. Gunel, K. Lu, G. Scott and S. Conolly, "Optimal Broadband Noise Matching to Inductive Sensors: Application to Magnetic Particle Imaging," *IEEE Transactions on Biomedical Circuits and Systems*, vol. 11, no. 5, pp. 1041-1052, 2017.

[27] B. Zheng, "System Hardware and in vivo Cell Tracking in Magnetic Particle Imaging," *UC Berkeley Thesis and Dissertation*, University of California, Berkeley, 2015.

[28] Analog Devices, "Low Noise, 1 GHz FastFET Op Amps," ADA4817 Datasheet, 2008.

[29] J. Sevick, "A Simplified Analysis of the Broadband Transmission Line Transformer," *High Frequency Electronics*, February 2014.

[30] Texas Instruments, "Wideband, Ultra-Low Noise, Voltage-Feedback OPERATIONAL AMPLIFIER with Shutdown," OPA847 Datasheet, 2022.

[31] H. T. Friis, "Noise Figures of Radio Receivers," *Proceedings of the IRE*, vol. 32, no. 7, pp. 419-422, July 1944.